Mechanics of Materials 209 (2025) 105442

Contents lists available at ScienceDirect

Mechanics of Materials

journal homepage: www.elsevier.com/locate/mecmat

Research paper

A strain energy function for the inflation of hyperelastic membranes

Stefano Sirotti [a,*], Matteo Pelliciari [a], Angelo Aloisio [b], Angelo Marcello Tarantino [a]

[a] DIEF, Department of Engineering "Enzo Ferrari", via P. Vivarelli 10, 41125 Modena, Italy
[b] Department of Civil, Construction-Architectural and Environmental Engineering, Università degli Studi dell'Aquila, L'Aquila, 67100, Italy

ARTICLE INFO

Keywords:
Deviatoric SEF
Bulge tests
Softening
Compressibility
Nonlinear elasticity
Nonlinear fitting

ABSTRACT

We propose a deviatoric strain energy function (SEF) for inflated elastic membranes. The proposed function is specifically designed to capture the essential features of the pressure-deflection response of circular membranes. The model parameters are calibrated on pressure-deflection data obtained from bulge tests performed on two different elastomers. Besides the pressure curve, we measure the transversal stretch and radial stretch at the membrane's pole, as well as the deformed profiles. These data are used to further validate the proposed SEF, demonstrating that it overcomes the limitations of current models in accurately simulating both the mechanics and kinematics of inflated membranes. In addition, the proposed SEF offers several advantages: (1) a simple polynomial expression, (2) a clear interpretation of each term's role on the pressure response, and (3) a well-defined strategy for parameter fitting. Combined with a volumetric SEF previously developed by the authors, the proposed function forms a complete SEF for modeling the inflation of compressible membranes. This study helps bridge a gap in the literature by providing original experimental insights and theoretical advancements in the modeling of inflated membranes.

1. Introduction

Inflated membranes are capable to withstand large elastic deformations. For this reason, they find application in several technological fields, such as structural and aerospace engineering (Ma et al., 2018; Huntington, 2013; Jenkins, 2001; Jones, 2014), electronics (Stewart and Sitaraman, 2021; Liu et al., 2021), biomechanics (Murphy and Rajagopal, 2021; Takashima et al., 2007; Serina et al., 1998), soft robotics (Gorissen et al., 2019; Chen et al., 2019; Walker et al., 2020) and energy storage (Yazdi et al., 2020). Inflated membranes are typically made of elastomers, but in recent years innovative materials such as foams (Vandeparre et al., 2013; Doutres et al., 2011; Hailan et al., 2021) and gels (Tamura et al., 2011; Wang and Zhang, 2014; Ma et al., 2019) have become increasingly popular.

The scientific interest towards inflated membranes demands for a deep understanding of their mechanical behavior. However, the strong nonlinearities involved forced researchers to adopt mainly numerical approaches to solve problems of inflated membranes. As early as 1952, Adkins and Rivlin derived the solution of the benchmark problem of the inflation of a circular membrane (Adkins and Rivlin, 1952). Since then, numerous researchers developed numerical approaches for more complex problems, involving contact mechanics (Patil et al., 2015; Liu et al., 2018), pre-stretched membranes (Patil and DasGupta, 2013; Chaudhuri and DasGupta, 2014) and different geometries (Tamadapu and DasGupta, 2014; Reddy and Saxena, 2017).

The experimental investigation and analytical modeling of inflated membranes still have extensive gaps. The simplest experimental test is the bulge test, namely the inflation under lateral pressure of an initially flat circular membrane, and it was performed in many studies. However, most of them focused on measuring the inflating pressure and the deflection of the pole (Sheng et al., 2017; Pelliciari et al., 2022). Only a few works provided information on the deformed configurations of the membrane or on the strain field in the material. Li et al. (2001) monitored the deformed shape by a high-speed optical measurement system placed above the membrane. Pamplona and Mota (2012) investigated the response of a skin-like elastomeric membrane inflated over a rigid and an elastic foundation, monitoring the deformed shape by a lateral camera. Machado et al. (2012) developed a procedure to reconstruct the surface curvatures from 3D-Digital Image Correlation (DIC) measurements, subsequently deriving the stress and strain fields along the membrane profile. However, in all these works the deformations attained are relatively small, and the material behavior is simulated by the simple Neo-Hookean and Mooney–Rivlin models.

On the other hand, analytical solutions for the inflation of a circular membrane can be found only under simplified assumptions. Fichter

* Corresponding author.
E-mail addresses: stefano.sirotti@unimore.it (S. Sirotti), matteo.pelliciari@unimore.it (M. Pelliciari), angelo.aloisio1@univaq.it (A. Aloisio), angelomarcello.tarantino@unimore.it (A.M. Tarantino).

https://doi.org/10.1016/j.mechmat.2025.105442
Received 16 April 2025; Received in revised form 1 July 2025; Accepted 13 July 2025
Available online 24 July 2025

(1997) derived an approximate solution based on aseries expansion, assuming small strains and linear elastic material. Yang et al. (2021) derived a closed-form solution for Neo-Hookean materials assuming very large strains. Yuan et al. (2021) proposed a solution for incompressible Mooney–Rivlin materials assuming spherical deformed configurations. In previous works (Pelliciari et al., 2022; Sirotti et al., 2023), we developed an approximate analytical solution for unstretched and pre-stretched Mooney–Rivlin membranes. However, as highlighted by experimental tests, the Mooney–Rivlin model was inadequate to capture the complex response of inflated membranes.

The constitutive models commonly adopted in inflated membrane problems suffer from significant limitations. They are typically calibrated using simpler tests, such as uniaxial tension, which do not represent the complex mechanical behavior of inflated membranes. In addition, simple models are often used to simplify mathematical formulations and computations. As a result, there is no guarantee that these models can accurately capture important phenomena observed in inflated membranes. In particular, their performance near limit-point instabilities and under very large deformations is often not thoroughly assessed. Moreover, their predictions of strain quantities and kinematics are often neglected or rarely validated against experimental measurements.

Lastly, there is lack in the literature of experimental and analytical studies on membranes involving material compressibility. This is due to the fact that elastomers are typically modeled as incompressible materials, as their bulk modulus is much larger than their shear modulus. However, in agreement with previous authors (Blatz and Ko, 1962; Starkova and Aniskevich, 2010), we showed in Pelliciari et al. (2023) that large volume changes can occur in some kind of elastomers, especially at large deformations. In Sirotti et al. (2024), we showed numerically the impact that compressibility can have on the mechanical response of inflated membranes. Despite our efforts, this last study lacked an experimental investigation aimed at determining the actual volume changes occurring in the membranes.

In light of the above considerations, this work brings several contributions in the experimental investigation and analytical modeling of inflated circular membranes. Firstly, we perform comprehensive bulge tests on two kinds of elastomer. These materials were previously tested in simple tension in Pelliciari et al. (2023), where their volumetric properties were characterized by a novel volumetric SEF. Besides the pressure curve, during the bulge tests we perform measurements of kinematics quantities to provide a comprehensive characterization of the membranes' response. Specifically, we reconstruct the deformed shapes and the radial stretch at the pole of the membrane by recording the test using a lateral and an upper camera, respectively. Furthermore, two lasers are employed to measure the transversal deformation at the pole of the membrane. This data provides information on the volume changes occurring at the pole and, to the best of the authors' knowledge, it is the first time this has been reported in the literature.

The hyperelastic model for inflated membranes is developed adopting the split of the energy function into its deviatoric and volumetric parts. The function proposed in Pelliciari et al. (2023) is assumed as volumetric SEF. To choose a suitable deviatoric SEF, we select the most popular current deviatoric SEFs in the literature and examine their effectiveness by fitting the experimental data. We show that all current models exhibit limitations in accurately simulating the experimental response of inflated membranes. Consequently, we propose a novel deviatoric SEF to overcome the limitations of current models. The proposed model is fitted to the experimental data and proves excellent accuracy in capturing the pressure vs. deflection curves as well as the kinematics quantities.

To resume, the main innovations of this work are the following: (1) a novel deviatoric SEF specifically calibrated for inflated membranes, (2) comprehensive bulge tests of circular membranes, with the measurements of radial and transversal stretch at the pole, and (3) experimental validation of the volumetric SEF previously proposed in Pelliciari et al. (2023), which effectively captures the volume changes occurring in the material. These contributions extend and deepen the overall understanding of the mechanics of inflated membranes, expanding the potential applications of these structures as soft actuators, sensors, energy harvesters and biomedical devices.

The paper is organized as follows. In Section 2, we recall basic concepts in the modeling of hyperelastic materials. In Section 3, we present the characterization of the materials considered and the bulge tests performed. In Section 4, we review some of the most popular deviatoric SEFs in the literature and we show their limitations in the modeling of inflated membranes. Based on these issues, in Section 5 we propose an original deviatoric SEF specifically designed for inflated membranes. In Section 6 we fit the proposed SEF to the experimental data, discussing the results. Conclusions are drawn in Section 7.

2. Theoretical background

The mechanical behavior of a hyperelastic material derives from the definition of a strain energy function W. Under the assumption of frame-indifference and isotropy, W is a symmetric function of the principal strain invariants (Upadhyay et al., 2019), namely

$$W = W(I_1, I_2, I_3), \tag{1}$$

with I_1, I_2 and I_3 defined as

$$\begin{aligned} I_1 &= \mathrm{tr}\mathbf{B} = \lambda_1^2 + \lambda_2^2 + \lambda_3^2, \\ I_2 &= \frac{1}{2}\left[(\mathrm{tr}\mathbf{B})^2 - \mathrm{tr}\left(\mathbf{B}^2\right)\right] = \lambda_1^2\lambda_2^2 + \lambda_1^2\lambda_3^2 + \lambda_2^2\lambda_3^2, \\ I_3 &= \det\mathbf{B} = \lambda_1^2\lambda_2^2\lambda_3^2, \end{aligned} \tag{2}$$

where $\mathbf{B} = \mathbf{F}\mathbf{F}^T$ is the left Cauchy–Green deformation tensor, $\mathbf{F}$ is the deformation gradient, and λ_1, λ_2 and λ_3 are the principal stretches. The Cauchy stress tensor describes the stress in the deformed configuration and can be written as (Ogden, 1997)

$$\mathbf{T} = \beta_0\mathbf{I} + \beta_1\mathbf{B} + \beta_{-1}\mathbf{B}^{-1}, \tag{3}$$

where β_0, β_1, and β_{-1} are functions of the principal invariants given by

$$\beta_0 = \frac{2}{\sqrt{I_3}}\left(I_2\frac{\partial W}{\partial I_2} + I_3\frac{\partial W}{\partial I_3}\right), \quad \beta_1 = \frac{2}{\sqrt{I_3}}\frac{\partial W}{\partial I_1}, \quad \beta_{-1} = -2\sqrt{I_3}\frac{\partial W}{\partial I_2}. \tag{4}$$

Elastomers are typically modeled as incompressible materials, based on the observation that their bulk modulus is much larger than their shear modulus. However, several researchers brought experimental evidence of significant volume changes in certain types of elastomers, in particular when large deformations are involved (see, e.g., Pelliciari et al., 2023; Blatz and Ko, 1962; Starkova and Aniskevich, 2010 and Kugler et al., 1990). Since we are interested in a comprehensive description of the response of elastic membranes, including the kinematics of deformation, we consider the general case of compressible materials. To this purpose, we adopt the split of the strain energy function (Sansour, 2008; Moerman et al., 2020):

$$W = W_d\left(\bar{I}_1, \bar{I}_2\right) + W_h\left(J\right), \tag{5}$$

where $J = \sqrt{I_3} = \det\mathbf{F}$ and $\bar{I}_1 = J^{-2/3}I_1$, $\bar{I}_2 = J^{-4/3}I_2$ are the so-called deviatoric strain invariants. The strain energy is now decomposed into two uncoupled terms, W_d and W_h, responsible respectively for the deviatoric and volumetric deformations. Consequently, the Cauchy stress tensor can be expressed as $\mathbf{T} = \mathbf{T_d} + \sigma_h\mathbf{I}$, with

$$\sigma_h = \frac{1}{3}\mathrm{tr}\mathbf{T} = \frac{\mathrm{d}W_h}{\mathrm{d}J}. \tag{6}$$

In Pelliciari et al. (2023), we investigated the volume changes arising in elastomers at large deformations and proposed a volumetric SEF specifically calibrated for the volumetric deformations of elastomers. The volumetric SEF is expressed by $W_h(J) = \kappa\left[H(1-J)\Psi_c(J) + H(J-1)\Psi_t(J)\right]$, where κ is the bulk modulus, H is the Heaviside step function and Ψ_c, Ψ_t are functions regulating respectively the response

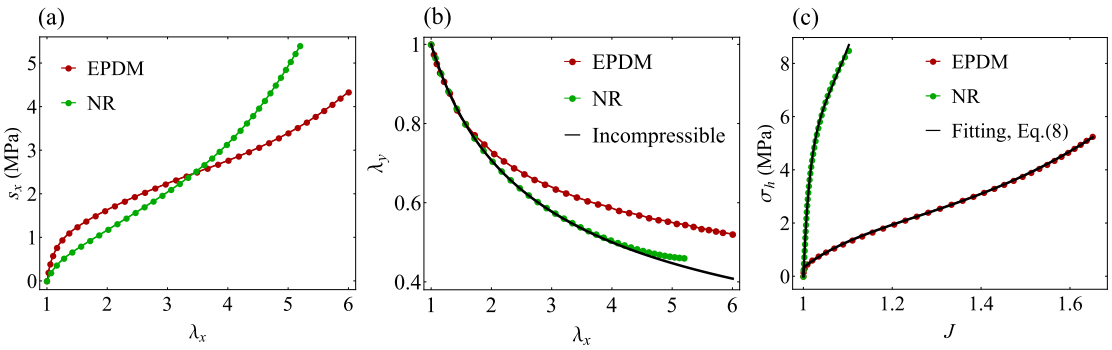

Fig. 1. Experimental data from simple tension tests on EPDM and NR. (a) Nominal stress vs. longitudinal stretch, (b) lateral stretch vs. longitudinal stretch and (c) hydrostatic stress vs. volume change. The continuous black line in (b) represents the response of an incompressible material, $\lambda_y = 1/\sqrt{\lambda_x}$. The continuous black line in (c) represents the hydrostatic stress given by Eq. (8), whose parameters are reported in Table A.2. A detailed description of the experiments can be found in Pelliciari et al. (2023).

for volume shrinkage and volume expansion. Since membranes can sustain only tensile stress, we restrict our interest to the case of volume expansion, where $J > 1$. Therefore, the volumetric SEF reduces to

$$W_h(J) = \kappa\Psi_t(J) = \kappa(1-q)\left[\frac{\beta_2 e^{\beta_1(J-1)} + \beta_1 e^{-\beta_2(J-1)}}{\beta_1\beta_2(\beta_1+\beta_2)} - \frac{1}{\beta_1\beta_2}\right] + \kappa q\beta_3^2 \ln\left(\cosh\left(\frac{J-1}{\beta_3}\right)\right), \tag{7}$$

whereas the hydrostatic stress σ_h is computed as

$$\sigma_h(J) = \frac{\mathrm{d}W_h}{\mathrm{d}J} = \kappa(1-q)\frac{e^{\beta_1(J-1)} - e^{-\beta_2(J-1)}}{\beta_1+\beta_2} + \kappa q\beta_3 \tanh\left(\frac{J-1}{\beta_3}\right). \tag{8}$$

In addition to the bulk modulus κ, the volumetric response is controlled by four parameters: $\beta_1, \beta_2, \beta_3$ and q. More details about the role of these parameters and the mathematical properties of the volumetric SEF can be found in Pelliciari et al. (2023). Henceforth, we assume Eq. (7) as volumetric part of the SEF. In the following section we present the bulge tests carried out on the elastomeric membranes. Successively, we seek a suitable function to assume as deviatoric part of the SEF to obtain a complete description of the mechanics of elastic membranes.

Remark 1. In the framework of the split of the SEF, the response of the material to purely volumetric deformations is completely described by the volumetric part W_h and it is independent from the deviatoric part W_d. Indeed, the parameters of W_h can be determined based solely on the volumetric curve σ_h vs. J by means of Eq. (6). In case of simple tension, we have $\mathrm{d}W_h/\mathrm{d}J = \sigma_h = \sigma_1/3$ and the hydrostatic stress can be fitted to the experimental data provided that volume changes are measured. The volumetric parameters determined in this manner characterize the material response to volume changes and they do not depend on the particular deformation.

3. Materials and experiments

In this section, we present the materials considered in our study and the bulge tests performed. First, we briefly summarize the materials characterization done in our previous work using simple tension tests. Subsequently, we provide a detailed description of the experimental setup for the bulge tests and discuss the results obtained.

3.1. Description of the materials considered

We analyzed two kinds of elastomers: EPDM (ethylene propylene diene monomer) and NR (natural rubber). In Pelliciari et al. (2023), we subjected both materials to uniaxial tensile tests monitoring their lateral deformation to characterize their stress vs. stretch response and their compressibility properties. The results are reported in Fig. 1.

Fig. 1(a) shows the nominal stress vs. stretch response. Both materials undergo very large stretches before failure, exhibiting the typical strain hardening effect due to the limit chain extensibility of polymers. Their capability to sustain large deformations makes these materials ideal for membrane applications such as energy harvesting and actuators (Koh et al., 2010; Li et al., 2013).

Fig. 1(b) shows the lateral stretch (λ_y) vs. longitudinal stretch (λ_x) curve. The continuous black line represents the behavior of an incompressible material, given by $\lambda_y = 1/\sqrt{\lambda_x}$. Despite being nearly incompressible at small strains, EPDM significantly deviates from the incompressible curve as the stretch increases, indicating a marked compressibility. Therefore, a compressible model is necessary for an accurate description of its response. In contrast, NR remains approximately incompressible over most of the deformation range, starting to deviate only at $\lambda_x \approx 5$.

Fig. 1(c) shows the volumetric curve in volume expansion for both materials. This curve was obtained by computing the hydrostatic stress as $\sigma_h = s_x/(3\lambda_y^2)$ and the volume change as $J = \lambda_x\lambda_y^2$. As EPDM reaches a maximum volume change of 60%, it is necessary to account for material compressibility in its modeling. In contrast, NR reaches a volume change of about 10%. An incompressible model would be a good approximation of this material. However, volume changes in the bulge test could be larger and become non-negligible. For this reason, we chose to adopt a compressible model for NR as well. In Pelliciari et al. (2023), we fitted the parameters of Eq. (8) to the volumetric curve for both EPDM and NR. The fitted curves are represented by the continuous lines in Fig. 1(c) and the optimal parameters are listed in Table A.2. These parameters comprehensively characterize the materials' response to volume changes and will remain fixed in the subsequent analyses.

3.2. Bulge tests setup

Four membrane specimens of thickness $H = 2$ mm were prepared for both EPDM and NR. As depicted in Fig. 2(a), a custom-built steel device was used for the bulge tests. It consists of a hollow cylinder, closed at the bottom, with a flanged cap at the top that features a 40 mm radius hole for positioning the circular membrane specimen.

The device functions as a pressure tank with three openings. At the top opening, a Trafag International NAH8254 pressure sensor (0–10 bar range, 0.03 bar precision) measures the internal pressure. The central 5 mm diameter opening allows airflow from a compressor through a gun equipped with a manometer. A screw-type regulator controls the flow, ensuring quasi-static test execution. The bottom opening transmits data from a Microepsilon optoNCDT ILD1420-500 laser sensor (100–600 mm range, 0.01 mm accuracy), which is aligned orthogonally to the membrane's pole. During inflation, the laser tracks its displacement, providing deflection data of the membrane's pole. Both pressure and laser signals are acquired using a PXI-based data acquisition system operating at a 10 kHz sampling rate, ensuring accurate detection of potential instabilities during quasi-static inflation.

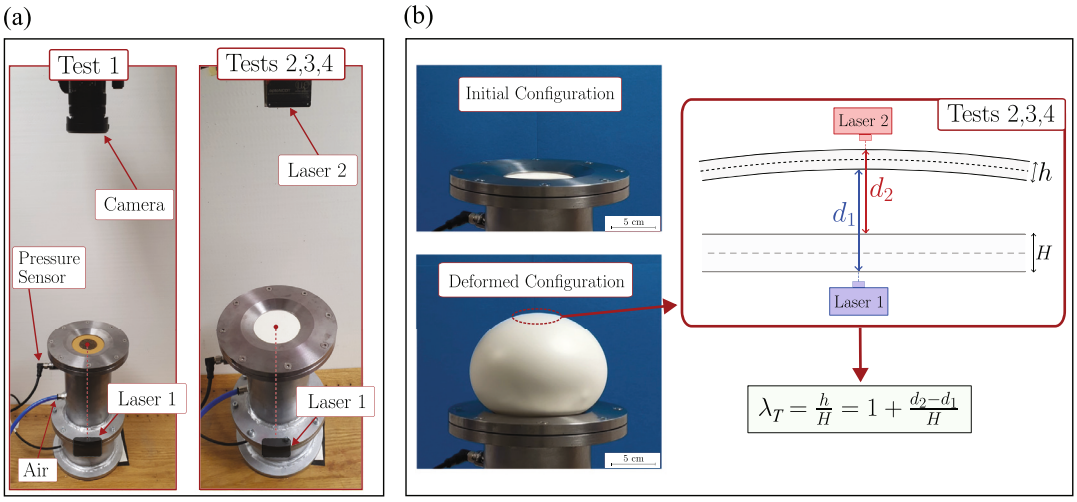

Fig. 2. Bulge tests on EPDM and NR circular membranes. (a) Experimental setup. During the first test, a camera orthogonally placed above the membrane recorded the test. The radial stretch λ_R at the pole was computed by DIC post-processing, as described in Appendix B.1. In addition, a second camera was used to record the test from a lateral orthogonal view, reconstructing the deformed shapes as described in Appendix B.2. During the remaining three tests, the camera at the top was replaced by a second laser to measure the variation in thickness at the pole. (b) Initial and deformed configurations as recorded by the lateral camera and schematization of the computation of transversal stretch λ_T at the pole. Laser 1 and 2 measure their distance from the lower and upper surface of the membrane, respectively. The displacements of these surfaces, respectively d_1 and d_2, are directly obtained from these measurements and the transversal stretch at the pole is computed.

For the first test on both materials, two cameras were installed to record videos of the tests and derive information on the deformation of the membrane. One camera was placed above the membrane, aligned orthogonally to the initially flat membrane and centered on the pole. By performing a DIC post-processing on MATLAB, described in detail in Appendix B.1, we computed λ_R, the stretch in the radial direction at the pole of the membrane. The second camera was placed in front of the membrane to capture a lateral orthogonal view of the test. As described in Appendix B.2, the video was again post-processed on MATLAB to reconstruct the deformed shapes of the membrane during the test.

During the remaining three tests, the cameras were removed and a second laser, identical to the one described above, was installed above the membrane, maintaining the same orthogonal alignment and central positioning. The two lasers, placed below and above the membrane, measured their respective distance from the membrane's surfaces during the test. These measurements provided the displacement of the lower and upper surfaces, denoted as d_1 and d_2 respectively. The transversal stretch at the pole of the membrane was then calculated as $\lambda_T = 1 + (d_2 - d_1)/H$. A schematic representation of this computation is given in Fig. 2(b).

3.3. Bulge tests results

The results of the bulge tests are shown in Fig. 3. The pressure vs. pole's deflection curves are depicted in Fig. 3(a) and (d) in terms of normalized pressure $\bar{p} = pL/H$ and normalized deflection $\bar{\delta} = \delta/L$, where $H = 2$ mm and $L = 40$ mm are the membrane thickness and radius, respectively. The variation among the four tests was minimal for both EPDM and NR, so we will consider their average in the subsequent analyses.

The pressure vs. deflection curve for EPDM exhibits a limiting pressure point around $\bar{\delta} = 1.5$ followed by a softening branch. The pressure then rises again due to the limiting chain extensibility of polymers, until failure. In contrast, the pressure curve for NR does not show a softening branch. After the characteristic abrupt decrease in stiffness around $\bar{\delta} = 1$, the curve remains monotonic with pressure nearly constant. At very large strains, the curve stiffens again until failure. These represent the two typical pressure responses of inflated membranes. A hyperelastic model specifically designed for inflated membranes must accurately reproduce both.

Fig. 3(b) and (e) show the λ_R vs. $\bar{\delta}$ curve for EPDM and NR, respectively. It is interesting to observe the strong correspondence between the ultimate stretch attained during the bulge test and that reached in simple tension test for both material. This result may seem counterintuitive, since the bulge test subjects the material to a biaxial stress state, which is more demanding than the uniaxial stress state in simple tension test. However, this result suggests that failure occurs when the materials' fibers attain their ultimate stretch, regardless of the stress required to reach this condition. This result agrees with what was observed for the graphene-based polymer nanocomposite inflated membranes studied in Pelliciari et al. (2025).

Finally, Fig. 3(c) and (f) display the λ_T vs. $\bar{\delta}$ curves for EPDM and NR. For both materials the measurements recorded during the three tests showed little variations in the range of small and moderate values of deflection. For large values of deflection, the measurements registered increasing discrepancies, particularly marked for NR. At large strains, the thickness of the membrane reduces significantly, affecting the accuracy of the instrumentation and causing inconsistent measurements. This happens mainly because the significant thinning of the membrane reduces the quality of the reflected laser signal and may lead to partial light penetration. Additionally, progressive polymer crystallization during stretching can locally alter the surface optical properties, further degrading the measurement. These combined effects, along with the intrinsic limitations of the sensor, are believed to contribute to the observed noise.

In the next section, we examine the effectiveness of current deviatoric SEFs in modeling the response of inflated membranes by fitting their parameters to the experimental data discussed above. We decided to include only the pressure vs. deflection data in the fitting procedure, as it is the most accurate measurement and the most relevant data from a practical standpoint. Moreover, it allows for the definition of a clear objective function to be minimized. Successively, we utilize the λ_R vs. $\bar{\delta}$ and the λ_T vs. $\bar{\delta}$ curves as an a posteriori check to evaluate the ability of these models to provide a comprehensive description of the mechanics of inflated membranes. On the other hand, due to the high nonlinearity of the problem, it is unlikely to obtain a perfect representation of the deformed configuration of the membrane with just a small amount of parameters contained in the SEF. In addition, in previous works (see Pelliciari et al. (2022)) we observed that minimal discrepancies in the deformed shapes can lead to significant errors in the pressure vs.

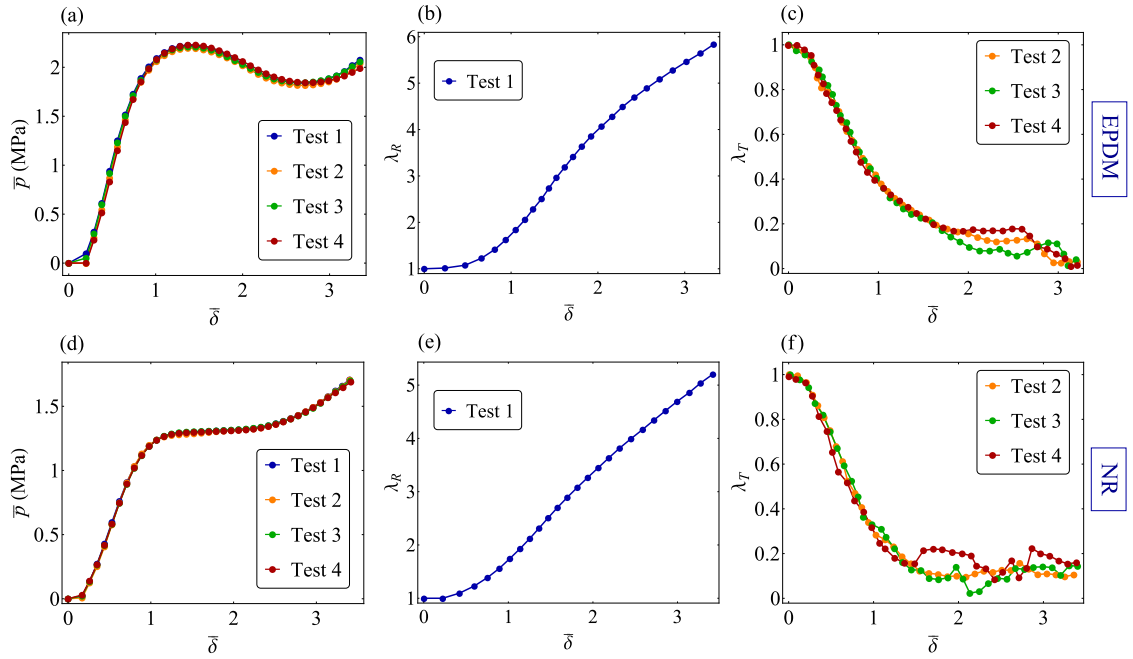

Fig. 3. Experimental curves from bulge tests on EPDM (Figs. (a), (b) and (c)) and NR (Figs. (d), (e) and (f)) circular membranes: (a), (d) normalized pressure $\bar{p} = pL/H$ vs. normalized deflection $\bar{\delta} = \delta/L$; (b), (e) radial stretch at the pole λ_R vs. $\bar{\delta}$ and (c), (f) transversal stretch at the pole λ_T vs. $\bar{\delta}$. The discrepancies in the measurements of λ_T at large values of deflection are due to the significant reduction in membrane thickness.

deflection curve. Therefore, we do not involve the deformed shapes in the evaluation of the accuracy of current SEFs. We rather consider the experimental deformed shapes in Section 6 for a qualitative validation of the deformed shapes obtained by our proposed model.

4. Limitations of current deviatoric SEFs

In recent decades, several researchers have proposed SEFs to simulate the large deformations of elastomers. However, determining a formulation capable of making accurate predictions across the widest possible range of loading conditions remains an open problem. In this work, we do not aim to address this issue. Instead, our focus is on identifying a suitable SEF for inflation problems of elastic membranes, ensuring that it captures their essential mechanical features. Moreover, we restrict our attention to isotropic materials, although the modeling of anisotropic behavior is gaining increasing interest (Borjalilou and Asghari, 2022; Sedighi et al., 2021).

In the following, we examine some of the most popular deviatoric SEFs available in the literature. We demonstrate that each model has limitations in accurately simulating the experimental response of inflated membranes and we identify some key features that the deviatoric SEF should possess for an accurate modeling of this problem. Moving from these considerations, in the next section, we propose a deviatoric SEF specifically designed for the inflation of elastic membranes.

Remark 2. The formulations we examine were introduced in the context of incompressible hyperelasticity as functions of the principal invariants I_1 and I_2. In case of compressible materials, these models represent the deviatoric part of the SEF, provided that the principal invariants I_1 and I_2 are replaced with the deviatoric invariants $\bar{I}_1$ and $\bar{I}_2$. Since we adopted the split of the SEF, in the following discussion we will write these models as functions of $\bar{I}_1$ and $\bar{I}_2$ and we will refer to these models as deviatoric SEFs. In case of a SEF written as function of the principal stretches λ_i, these are replaced by the deviatoric stretches defined as $\bar{\lambda}_i = J^{-1/3}\lambda_i$.

Table 1
Current SEFs from the literature. We considered the most popular models with up to four parameters. Although these models were introduced for incompressible materials, we adopted them as deviatoric part W_d of the SEF for compressible materials, using the isochoric variables $\bar{I}_1$, $\bar{I}_2$ and $\bar{\lambda}$. In the analyses, these models were coupled with the volumetric SEF given by Eq. (7).

Formulation	W_d
Yeoh and Fleming (1997)	$\frac{A}{B}\left(1-e^{-B(\bar{I}_1-3)}\right)-C_{10}\left(I_m-3\right)\ln\left(1-\frac{\bar{I}_1-3}{I_m-3}\right)$
Mooney-Rivlin (Rivlin, 1948)	$C_1\left(\bar{I}_1-3\right)+C_2\left(\bar{I}_2-3\right)$
Carroll (2011)	$A\bar{I}_1+B\bar{I}_1^4+C\sqrt{\bar{I}_2}$
Gent-Gent (Pucci and Saccomandi, 2002)	$-C_1J_m\ln\left(1-\frac{\bar{I}_1-3}{J_m}\right)+C_2\ln\left(\frac{\bar{I}_2}{3}\right)$
Ogden (1972)	$\sum_{i=1}^{M}\frac{\mu_i}{\alpha_i}\left(\bar{\lambda}_1^{\alpha_i}+\bar{\lambda}_2^{\alpha_i}+\bar{\lambda}_3^{\alpha_i}-3\right)$

4.1. Review of current deviatoric SEFs

The deviatoric SEFs considered in this study are listed in Table 1. The Yeoh-Fleming model (Yeoh and Fleming, 1997) combines concepts of the classic Yeoh and Gent models to achieve accurate simulations across both small and large strains. The model is solely function of the first invariant $\bar{I}_1$ and it involves four parameters. In Pelliciari et al. (2023), we identified the Yeoh-Fleming model as the most accurate deviatoric SEF for reproducing the response of EPDM and NR under simple tension. For this reason, it is considered the primary candidate for the deviatoric SEF in the response of inflated membranes.

The Mooney–Rivlin model (Rivlin, 1948) has a linear dependence on both the first and second strain invariants, and involves two material parameters. The inclusion of the $\bar{I}_2$ term in the SEF introduces deviations from molecular theory predictions. It is well known that this model is not effective at large strains, as it does not capture the strain hardening resulting from the limiting chain extensibility of polymers (Pelliciari et al., 2022; Sirotti et al., 2023). However, it provides good accuracy at small and moderate strains. Its mathematical

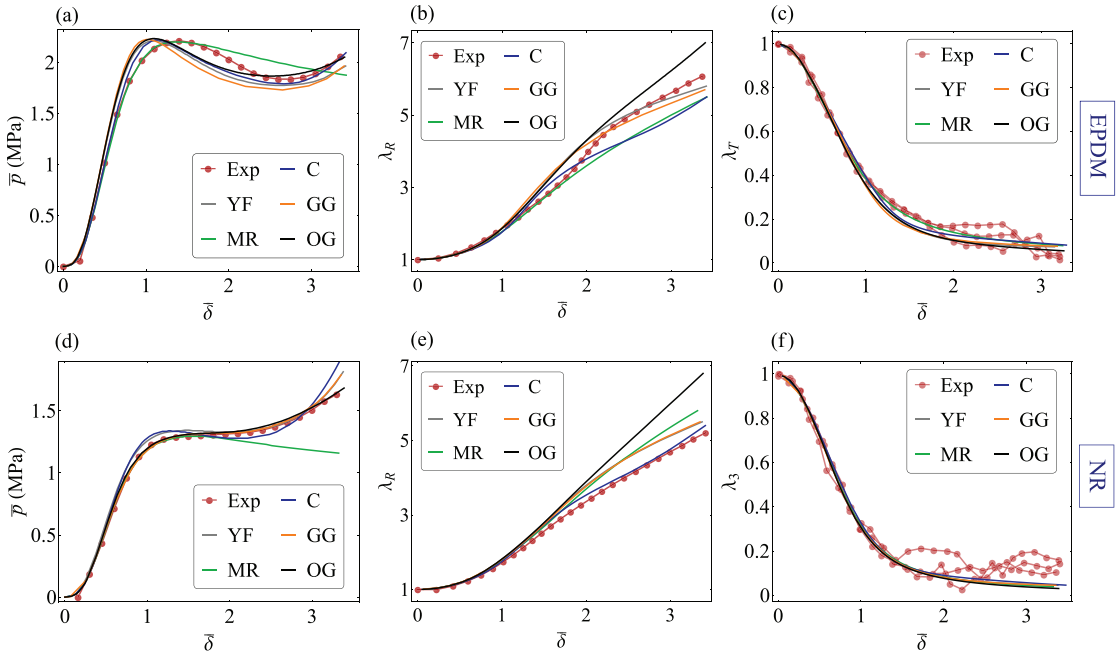

Fig. 4. Fitting of current SEFs to experimental data on EPDM (Figs. (a), (b) and (c)) and NR (Figs. (d), (e) and (f)) in terms of (a), (d) normalized pressure $\bar{p} = pL/H$ vs. normalized deflection $\bar{\delta} = \delta/L$; (b), (e) radial stretch at the pole λ_R vs. $\bar{\delta}$ and (c), (f) transversal stretch at the pole λ_T vs. $\bar{\delta}$. The following acronyms are used: Exp = Experimental data; YF = Yeoh and Fleming (1997); MR = Rivlin (1948); C = Carroll (2011); GG = Gent-Gent (Pucci and Saccomandi, 2002); OG = Ogden (1972).

simplicity has made it one of the most widely used models in the literature.

The model proposed by Carroll (2011) was derived on a phenomenological basis. It is composed by a neo-Hookean term enriched with two terms added to capture the residual stress in simple and equibiaxial extensions. In particular, it exhibits a dependence on the second invariant expressed as $\sqrt{\bar{I}_2}$. From a molecular-based standpoint, this $\bar{I}_2$ term arises by the constrained cross section approach of the topological tube model (Miehe et al., 2004; Khiêm and Itskov, 2016). Despite having only three parameters, it has proven effective in modeling the nonlinear deformations of elastomers across all strain ranges.

The Gent-Gent model is another popular three-parameter model. It was introduced by Pucci and Saccomandi (2002) by adding a logarithmic function of $\bar{I}_2$ to the classic Gent model to improve its accuracy in the range of small and moderate deformations. This term comes from the rational approximation of the response function (Anssari-Benam, 2021; Horgan and Saccomandi, 2002). Finally, we considered the well-known Ogden model (Ogden, 1972; Kuznetsov, 2024). This model is written as a sum of terms depending on the principal stretches raised to variable powers. For this study, we adopted the two-term Ogden model, consisting of four parameters.

4.2. Fitting of current deviatoric SEFs to experimental data

The current deviatoric models listed in Table 1 were coupled with the volumetric function given by Eq. (7) to obtain the complete SEFs. Then, for each SEF we solved the boundary value problem for the inflation of a circular membrane. Finally, we performed a parameter fitting to determine for each model the set of deviatoric parameters that best matches the experimental data. Appendix C reports the numerical solution for the inflation of circular membranes and details on the fitting procedure for the optimization of material parameters. As noted in Section 3, the fitting procedure was performed on the experimental $\bar{p}$ vs. $\bar{\delta}$ curve.

We remark that nonlinear fitting can easily lead to computational challenges, mainly due to the existence of multiple local minima and the need for an appropriate initial guess for the parameters (Destrade et al., 2017; Ogden et al., 2004). Here the fitting procedure is further complicated by the nature of the function being minimized. Specifically, the pressure vs. deflection curve derives from a system of differential equations that must be solved numerically for each set of parameters. This significantly increases computational complexity, highlighting the importance of models with parameters that are easy to control.

The results of each model are shown in Fig. 4. Specifically, Fig. 4(a) and (d) show the results of parameter fitting on the $\bar{p}$ vs. $\bar{\delta}$ curves. Most discrepancies were found in capturing the response of EPDM, particularly in the region around the limiting point. For the Yeoh-Fleming model, the errors in the limiting point region can be attributed to its lack of dependence on $\bar{I}_2$. While a sole dependence on $\bar{I}_1$ may be sufficient for accurately modeling certain stress states and offers mathematical simplicity, the need for an $\bar{I}_2$ term has been pointed out by several researchers, especially in case of biaxial stress states (Horgan and Smayda, 2012). From an experimental standpoint, as early as 1951, Rivlin and Saunders (1951) provided evidence of the strain energy function's dependence on $\bar{I}_2$ based on biaxial tests. More recently, this evidence has been reinforced by many studies (see, e.g., McKenna, 2018; Yohsuke et al., 2011; Kawabata and Kawai, 2005 and Falope et al., 2024). From a theoretical standpoint, the $\bar{I}_2$ terms arise naturally when molecular chain entanglements are incorporated into the molecular-based statistical treatment of rubber elasticity (Wagner, 1994). Furthermore, excluding the $\bar{I}_2$ terms from the strain energy function leads to a universal relation for biaxial deformation that is inconsistent with experimental data (Wineman, 2005; Anssari-Benam et al., 2021). For these reasons, the dependence on $\bar{I}_2$ is a necessary requirement for a consistent simulation of elastic membranes inflation.

The Carroll and the Gent-Gent models both incorporate a dependence on $\bar{I}_2$, expressed as $\sqrt{\bar{I}_2}$ and $\ln(\bar{I}_2/3)$, respectively. However, these functions do not lead to improvements in the limiting point region, suggesting that they are not suitable for modeling membranes' inflation. Moreover, these models have only three parameters, which are insufficient for accurate modeling across the full range of deformation.

Despite having four parameters, the Ogden model exhibits the same limitations of the previous models in simulating the response of EPDM. Nevertheless, it provides the most accurate simulation for the $\bar{p}$ vs. $\bar{\delta}$ curve of NR.

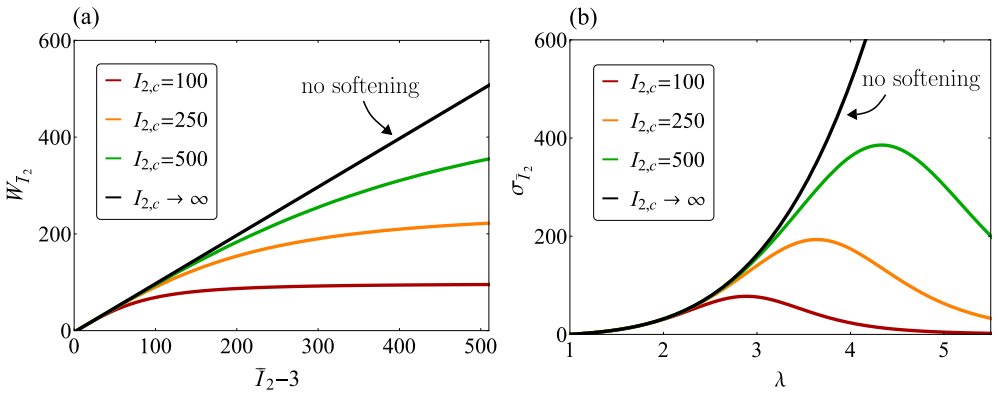

Fig. 5. Effect of softening on the $\bar{I}_2$ term of the proposed energy, $W_{\bar{I}_2} = B\,(\bar{I}_2 - 3)\,\phi_s$, normalized for $B = 1$. (a) Plot of $W_{\bar{I}_2}$ for different values of critical invariant $I_{2,c}$; (b) Plot of Cauchy stress $\sigma_{\bar{I}_2}$ vs. stretch in case of equibiaxial tension of an incompressible material. The stress $\sigma_{\bar{I}_2}$ derives from $W_{\bar{I}_2}$ and is computed as $\sigma_{\bar{I}_2} = 2(\lambda^4 - \lambda^{-2})\partial W_{\bar{I}_2}/\partial \bar{I}_2$.

Finally, the Mooney–Rivlin model provides strong accuracy in the region of small to moderate deformations for both EPDM and NR. The good agreement in this region is attributable to its linear $\bar{I}_2$ term. On the contrary, its linear dependence on both $\bar{I}_1$ and $\bar{I}_2$ prevents it from capturing strain hardening at large deformations. We remark that strain hardening should be governed by the invariant $\bar{I}_1$, since at the microscopic level it is connected to the finite extensibility of polymer chains (Gent, 2005). Moreover, the linear $\bar{I}_2$ term does not capture the softening branch that occurs for EPDM after the limiting point. Therefore, despite adjusting the limiting point region, the linear $\bar{I}_2$ term is not adequate to accurately simulate the response at large values of deflection.

Fig. 4(b) and (e) show the results in terms of λ_R vs. $\bar{\delta}$ curves. For EPDM, all the models considered exhibit significant discrepancies from the experimental data, especially at large deformations. In contrast, the behavior of NR is well captured by the Carroll model. However, note that the Ogden model, which provides the best simulation of the $\bar{p}$ vs. $\bar{\delta}$ curve, shows significant errors in terms of radial stretch. This could be related to the fact that the Ogden model's parameters are purely phenomenological and lack of physical interpretations, as already pointed out by other authors (Arruda and Boyce, 1993).

Finally, Fig. 4(c) and (f) show the results in terms of λ_T vs. $\bar{\delta}$ curves for EPDM and NR, respectively. For both materials, the simulations agree with the experimental data trends. Moreover, the simulated λ_T curves show minimal discrepancies across different models. This demonstrates that the deviatoric part W_d has little influence on the transversal stretch, which is instead primarily governed by the volumetric part W_h. This result further validates the adopted volumetric SEF given in Eq. (7), which was calibrated using volumetric curves obtained from simple tension tests.

The above discussion highlights some necessary characteristics of the deviatoric SEF to model the response of inflated membranes:

- The SEF should include a term dependent on $\bar{I}_2$, mainly responsible for the range of moderate deformations. A linear function of $\bar{I}_2$ is a suitable candidate for an accurate modeling in this range. However, the $\bar{I}_2$ term should decay at large deformations to reproduce the softening branch that may occur after the limiting pressure point.
- The SEF must be capable of reproducing the strain hardening occurring at large deformations due to the limiting chain extensibility of polymers. In particular, the hardening behavior at large strains should be governed solely by a $\bar{I}_1$ term.
- The SEF must be able to accurately model both behaviors of the pressure vs. deflection curve, namely when it exhibits a softening branch and when it is monotonic.

In the following section we propose a deviatoric SEF which possesses these characteristics and overcomes the limitations of current models.

5. The proposed deviatoric SEF

We propose a deviatoric strain energy function of the form

$$W_d\left(\bar{I}_1, \bar{I}_2\right) = A\left(\bar{I}_1 - 3\right) + B\left(\bar{I}_2 - 3\right)\phi_s\left(\bar{I}_2\right) + C\left(\bar{I}_1 - 3\right)^4, \tag{9}$$

where

$$\phi_s\left(\bar{I}_2\right) = \left[1 + \left(\frac{\bar{I}_2 - 3}{I_{2,c} - 3}\right)^2\right]^{-\frac{1}{2}} \tag{10}$$

is a function that introduces softening in the term $B(\bar{I}_2 - 3)$. This function comes from the concept of softening hyperelasticity developed by Volokh (2004, 2007, 2010) to model material failure within the framework of hyperelasticity. In Pelliciari et al. (2025), we extended this concept to model the effect of graphene nanoparticles on polymer composites. Eq. (10) corresponds to the model we proposed in Pelliciari et al. (2025) with $\beta = 2$.

The critical strain invariant $I_{2,c}$ defines a limiting value for the $\bar{I}_2$ term of the energy, $W_{\bar{I}_2} = B(\bar{I}_2 - 3)\phi_s$. Indeed, as $\bar{I}_2 \to \infty$, $W_{\bar{I}_2}$ tends to the constant value $B(I_{2,c} - 3)$. Conversely, when $I_{2,c} \to \infty$, function ϕ_s tends to unity and the softening effect vanishes. The effect of $I_{2,c}$ on $W_{\bar{I}_2}$ is shown in Fig. 5(a). To demonstrate the effect of softening on the stress, Fig. 5(b) shows the Cauchy stress $\sigma_{\bar{I}_2}$ vs. stretch under equibiaxial tension, condition that occurs at the pole. The stress $\sigma_{\bar{I}_2}$ derives from the $W_{\bar{I}_2}$ term of the strain energy function and is computed as $\sigma_{\bar{I}_2} = 2(\lambda^4 - \lambda^{-2})\partial W_d/\partial \bar{I}_2$, assuming for simplicity an incompressible material.

The deviatoric SEF proposed in Eq. (9) consists of three terms. Even though these terms are not independent, they primarily govern the pressure response in different regions, as shown in Fig. 6. Specifically:

- The linear $\bar{I}_1$ term governs the response at small and moderate strains. This term corresponds to the classic Neo-Hookean model and it provides an excellent fit as long as the deformation is small.
- The $\bar{I}_2$ term corrects discrepancies at moderate strains, particularly in the limiting point region. Note that $B(\bar{I}_2 - 3)$ is the Mooney–Rivlin $\bar{I}_2$ term, which provides great accuracy in this range of deformation (see Fig. 4). The function ϕ_s is necessary to introduce a reduction in this contribution after the limiting point, particularly when the pressure curve exhibits a softening branch. In addition, this ensures that the response at large strains is solely governed by $\bar{I}_1$.
- The fourth-power $\bar{I}_1$ term controls strain hardening at large deformations. A logarithmic term, as in the Yeoh-Fleming model, would be more theoretically sound, since it introduces a limiting stretch linked to the concept of limiting chain extensibility. However, we chose the $(\bar{I}_1 - 3)^4$ term for the following reasons: (1) the exponent at the fourth power effectively captures the strain

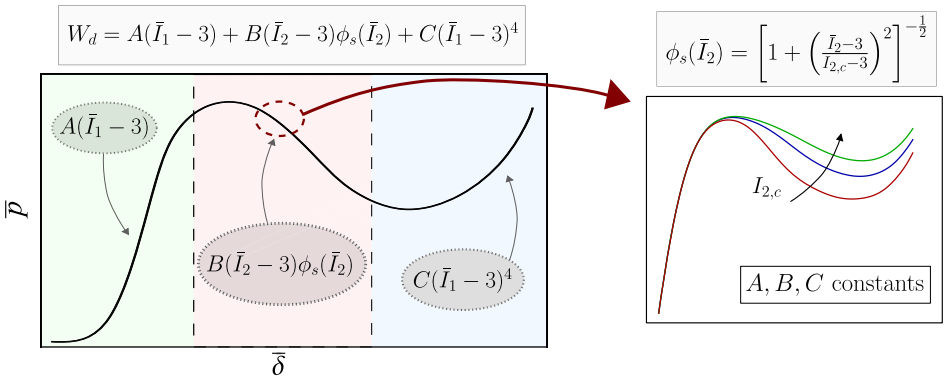

Fig. 6. Regions of influence of the terms of the proposed deviatoric SEF. The linear $\bar{I}_1$ term governs the behavior at small to moderate strains. The $\bar{I}_2$ term regulates the behavior at moderate strains near the limiting point, after which the function ϕ_s regulates the softening region. The fourth-power $\bar{I}_1$ term then controls strain hardening at large deformations. The right side of the figure shows the effect on the softening region as the value of $I_{2,c}$ increases.

hardening of polymers, as also observed by Carroll (2011) from a phenomenological approach, (2) its polynomial form simplifies numerical procedures, offering computational advantages and (3) contrary to the logarithmic term, the fourth power has minimal influence in the small-strains range, ensuring a clear separation of the contributions of each term simplifying the optimization process.

The proposed model counts for 4 parameters: A, B, $I_{2,c}$ and C. The critical strain invariant $I_{2,c}$ can be linked to a critical value of stretch λ_c, computed for simplicity by the relation $I_{2,c} = \lambda_c^4 + 2\lambda_c^{-2}$ for equibiaxial tension of an incompressible material. Although this relation is not exact for the considered membranes, it is a reasonable approximation which allows to link $I_{2,c}$ to experimental data. Specifically, by reading the stretch at the pole corresponding to the softening branch of the pressure curve, an initial estimate of λ_c can be obtained and subsequently refined by a fitting procedure.

Since the model parameters have a clear effect on the pressure curve, their calibration can be performed following a well-defined strategy:

(1) Firstly, parameters A and B are independently fitted based on the first branch of the pressure curve, up to the limiting point. During this step, $C = 0$ and $I_{2,c}$ is set to a sufficiently large value to avoid softening from occurring.
(2) Parameter C is then calibrated to capture the hardening rate of the final branch of the curve. Due to the fourth-power in the $\bar{I}_1$ term, variations of C do not affect the response up to the limiting point.
(3) Finally, the critical strain invariant $I_{2,c}$, or the critical stretch λ_c, is calibrated to obtain an optimal transition between moderate and large strains. As already observed, λ_c can be directly estimated from experimental data in case the measurement of the radial stretch is available.
(4) The set of parameters calibrated manually in the previous steps serves as initial guess for an optimization process aimed at refining the fitting accuracy. Details about the optimization process are found in Appendix C.

The simplicity of parameter calibration is a significant advantage of the proposed model. This is particularly important in the context of inflated membranes, where numerical procedures are typically required to solve the equilibrium equations. In the following section, the proposed model is fitted to the experimental data and the results are discussed.

Remark 3. To ensure physical plausibility, the range of model parameters is constrained by the conditions $A + B > 0$, $I_{2,c} > 3$ and $C > 0$. Nevertheless, the inclusion of the softening function ϕ_s may lead the proposed SEF to violate the Drucker stability criterion, $\partial^2 W / \partial \mathbf{F}^2 > 0$ (Boyce and Arruda, 2000), for certain parameter values and deformation ranges. As pointed out by other authors (Anssari-Benam, 2023; Destrade et al., 2017), there is no fundamental reason to rule out the possibility for the SEF to attain a negative tangent modulus during the deformation. This describes the phenomenon called *continuous* softening, i.e. a softening which takes place progressively in the primary loading path as the deformation increases (Anssari-Benam, 2023; Anssari-Benam and Saccomandi, 2024). Moreover, in membrane's inflation, we remark that a softening branch in the pressure vs. deflection curve does not necessarily imply a softening branch in the stress vs. stretch curve.

6. Fitting and discussion

As previously done in Section 4, the numerical solution to the inflation of a circular membrane for the proposed model was computed following Appendix C. We remark that the complete SEF is given by $W = W_d\left(\bar{I}_1, \bar{I}_2\right) + W_h(J)$, with W_d and W_h expressed by Eqs. (9) and (7) respectively. For both EPDM and NR, the parameters of W_h are known from their volumetric curve. The parameters of W_d were fitted on the experimental $\bar{p}$ vs. $\bar{\delta}$ curves and are listed in Table A.4. The results obtained from the proposed model are compared with the experimental data in Fig. 7.

The simulated $\bar{p}$ vs. $\bar{\delta}$ curve accurately fits the experimental one for both materials, as shown in Fig. 7(a) and (d). In particular, the proposed model successfully captures the response around the limiting point region for EPDM, overcoming the limitations of the existing formulations. This is due to the function ϕ_s introduced in the $\bar{I}_2$ term of the energy, which reduces this contribution allowing to properly simulate the softening branch, while preserving the accuracy at large strains given by the $\bar{I}_1^4$ term. Note that the optimal value $\lambda_c = 3.1$ corresponds to a deflection $\bar{\delta} \approx 1.6$, which actually falls within the softening branch of the $\bar{p}$ vs. $\bar{\delta}$ curve.

Fig. 7(b) and (e) show the simulated λ_R vs. $\bar{\delta}$ curves compared with experimental data. For EPDM, the curves exhibit discrepancies at large values of deflection, which are however reduced compared to the current formulations analyzed in Fig. 4(b). On the contrary, for NR the simulated λ_R vs. $\bar{\delta}$ curve matches the experimental one. This represents a significant improvement compared to existing formulations. In fact, as discussed in Section 4.2, the Gent-Gent model and the Ogden model simulate accurately the $\bar{p}$ vs. $\bar{\delta}$ curve but commit significant errors in the radial stretch λ_R.

Finally, the response in terms of λ_T vs. $\bar{\delta}$ curve is shown in Fig. 7(c) and (f). The simulated curve is accurate for both materials. This outcome was expected, since the transversal stretch is primarily governed by the volumetric part of the SEF, which had already demonstrated to be effective. This result confirms the ability of the adopted W_h to model

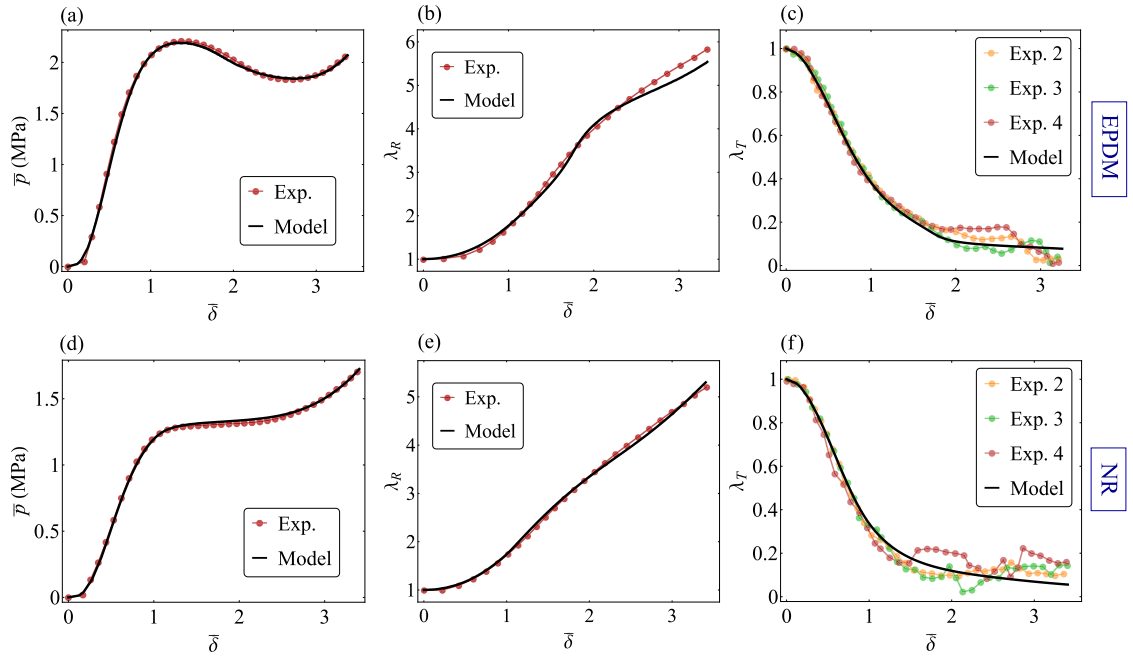

Fig. 7. Fitting of the proposed model to experimental data on EPDM (Figs. (a), (b) and (c)) and NR (Figs. (d), (e) and (f)) in terms of (a), (d) normalized pressure $\bar{p} = pL/H$ vs. normalized deflection $\bar{\delta} = \delta/L$; (b), (e) radial stretch at the pole λ_R vs. $\bar{\delta}$ and (c), (f) transversal stretch at the pole λ_T vs. $\bar{\delta}$. The proposed model corresponds to $W = W_d(\bar{I}_1, \bar{I}_2) + W_h(J)$, with W_d and W_h given respectively by Eqs. (9) and (7).

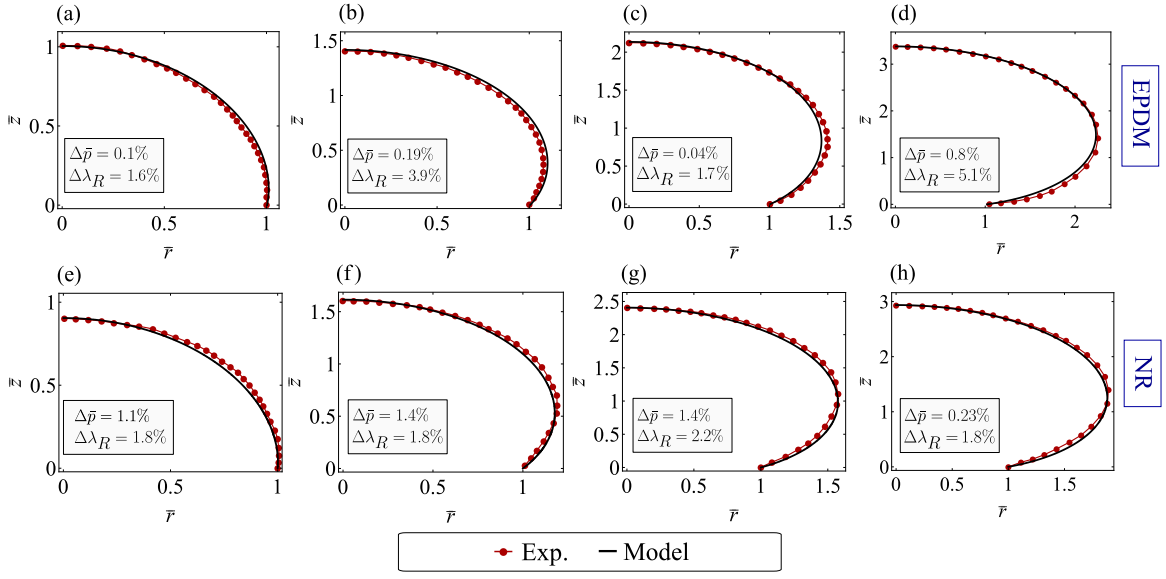

Fig. 8. Deformed shapes of EPDM (Figs. (a), (b), (c) and (d)) and NR (Figs. (e), (f), (g) and (h)) inflated membranes for different values of deflection at the pole. The deformed coordinates $\bar{r}$ and $\bar{z}$ are normalized with respect to L. The value $\bar{z}(0)$ corresponds to the normalized deflection $\bar{\delta}$. For each deformed shape, the error in pressure and in the radial stretch at the pole are computed, denoted respectively as $\Delta\bar{p}$ and $\Delta\lambda_R$.

the real volumetric behavior of the materials, regardless of the specific stress state.

Fig. 8 compares the deformed shapes predicted by the proposed model with those detected by the lateral camera during the bulge tests. The data processing and the reconstruction of the experimental deformed shapes are described in Appendix B. The comparison is made for the same values of deflection of the pole. The simulated deformed shapes are accurate throughout the entire inflation process. For clarity, in correspondence of each deformed shape we computed $\Delta\bar{p}$ and $\Delta\lambda_R$, representing the errors in terms of pressure and radial stretch at the pole. The error in pressure is minimal, as observed in Fig. 7(a) and (b). Although the error in terms of λ_R increases for EPDM at high values of deflection, it remains below approximately 5%.

We remark that, due to the highly nonlinear nature of the problem, capturing the entire mechanics and kinematics of membranes with a single four-parameter function, while fitting only the pressure curve, is not feasible. From this perspective, the results obtained by the proposed model are excellent, as a simple fitting of the pressure curve has also led to a highly accurate approximation of kinematic quantities as the stretches at the pole and the deformed shapes. This outcome is likely attributable to the clear physical interpretation associated with

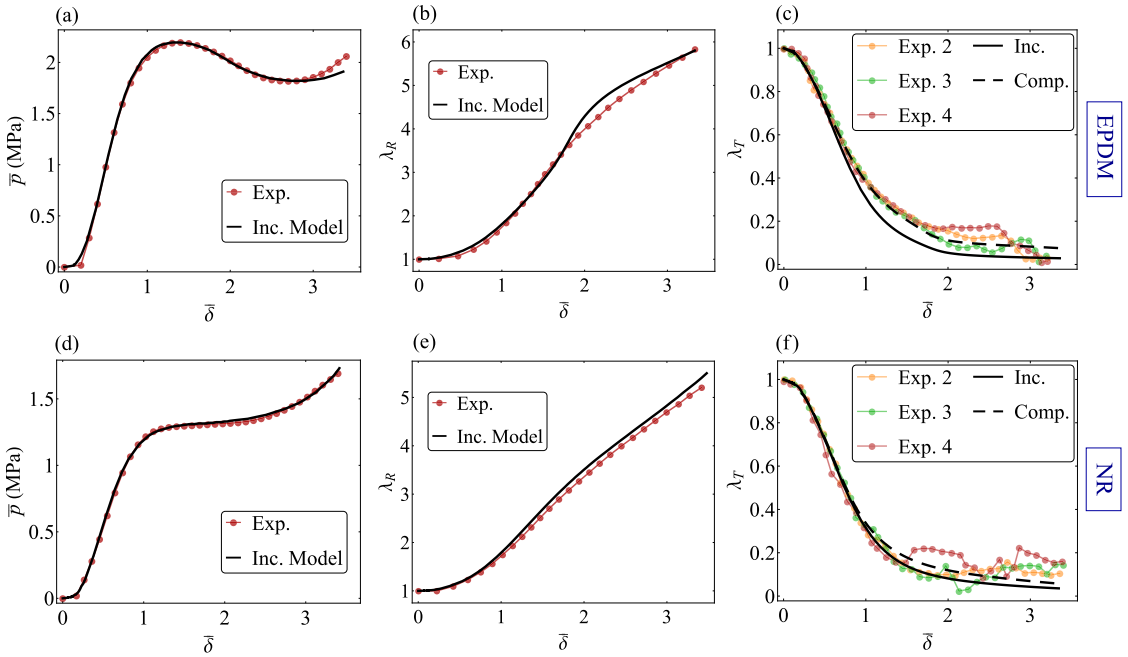

Fig. 9. Fitting of the proposed incompressible model, Eq. (11), to experimental data on EPDM (Figs. (a), (b) and (c)) and NR (Figs. (d), (e) and (f)) in terms of (a), (d) normalized pressure $\bar{p} = pL/H$ vs. normalized deflection $\bar{\delta} = \delta/L$; (b), (e) radial stretch at the pole λ_R vs. $\bar{\delta}$ and (c), (f) transversal stretch at the pole λ_T vs. $\bar{\delta}$. The black dashed lines in (c), (f) represent the compressible model, already reported in Fig. 7.

each parameter, which contributes to the robustness of the proposed hyperelastic formulation.

6.1. Incompressible materials

Since volume changes are negligible in most elastomers, it is natural to investigate the effectiveness of the proposed function in the case of material incompressibility and to compare the results of the incompressible model with the results of the compressible model shown in the previous section.

In case of incompressible materials, the deformation is isochoric, $I_3 = 1$, and the SEF is solely function of the first and second principal invariants of strain, $W = W(I_1, I_2)$. An incompressible material can be described by the proposed deviatoric SEF, provided the deviatoric invariants $\bar{I}_1$ and $\bar{I}_2$ are replaced by the classical principal invariants I_1 and I_2, obtaining the expression

$$W\left(I_1, I_2\right) = A\left(I_1 - 3\right) + B\left(I_2 - 3\right)\phi_s\left(I_2\right) + C\left(I_1 - 3\right)^4. \tag{11}$$

The boundary value problem for the inflation of an incompressible circular membrane was solved, assuming Eq. (11) as material model. The system of differential equations in case of incompressible material is derived in Appendix C.1. As done in the previous sections, the set of optimal parameters for the proposed incompressible model was determined by fitting the experimental $\bar{p}$ vs. $\bar{\delta}$ curves for both EPDM and NR, while the remaining data were used as validation. The optimal parameters are reported in Table A.5.

Fig. 9 shows the result of the fitting to the $\bar{p}$ vs. $\bar{\delta}$ curves, as well as the comparison in terms of λ_R vs. $\bar{\delta}$ and λ_T vs. $\bar{\delta}$ curves. For EPDM, the incompressible model accurately fits the pressure curve up to the hardening branch, where it begins to deviate. The radial stretch λ_R shows some discrepancies in reproducing the experimental response, though these errors are of the same magnitude as those observed in the compressible model. The most significant difference between the incompressible and compressible models is observed in the transversal stretch λ_T, as shown in Fig. 9(c). Specifically, the compressible model proves to be much more accurate in capturing the experimental measurements.

In the case of NR, material compressibility is less pronounced, therefore the results provided by the incompressible model align closely with those given by the compressible model. Specifically, the simulated $\bar{p}$ vs. $\bar{\delta}$ and λ_R vs. $\bar{\delta}$ curves are consistent with the experimental behavior. Minor discrepancies between incompressible and compressible models are found in the λ_T vs. $\bar{\delta}$ curve. The incompressible response seems to deviate from the average trend of experimental data, confirming the small compressibility arising at large deformations for NR.

The results of the proposed SEF applied to the case of incompressible membranes highlight the following two aspects:

- As shown in the pressure-deflection curve of EPDM in Fig. 9(a), compressibility has a direct impact on the pressure response. Specifically, the incompressible SEF fails to accurately reproduce the full pressure response of EPDM. In contrast, when volume changes are accounted for using the compressible formulation, as in Fig. 7(a), the model achieves excellent agreement with the experimental data. Hence, for materials exhibiting significant volumetric deformation, adopting an appropriate compressible model is essential.
- The proposed SEF is also effective for incompressible materials. Indeed for NR, which is nearly incompressible, the prediction remains equally accurate. This is a relevant observation, as incompressibility is a common assumption for most of elastomers. Therefore, the proposed SEF demonstrates robustness even when applied to incompressible membranes.

7. Concluding remarks

The analysis of circular inflated membranes lacks comprehensive experimental investigations and analytical modeling. In this work, we performed bulge tests on two kinds of elastomers, EPDM and NR, whose pressure vs. deflection responses represent the two typical behaviors of elastic membranes. In particular, EPDM shows a limiting point followed by a softening branch and strain hardening, whereas NR exhibits a monotonic trend. Besides the pressure curve, we measured the radial and transversal stretches at the pole of the membranes, as well as their

deformed shapes. These measurements represent a relevant novelty compared to previous experimental studies, which are typically limited to the pressure vs. deflection curve.

We have shown that the most popular SEFs in the literature fail to accurately simulate the experimental response of these materials. The most relevant limitations were found in modeling the limit point region and the subsequent softening branch in EPDM. For NR, the Ogden model fitted well the pressure curve, but it provided an unrealistic prediction of the radial stretch.

To address these shortcomings, we proposed a novel deviatoric SEF specifically designed for the inflation of membranes. The proposed SEF consists of three terms and counts for four parameters. Its advantages are: (1) mathematical simplicity, (2) clear effect of material parameters on the pressure curve and well-defined strategy for parameter fitting, and (3) accuracy for both typical responses of inflated membranes.

The proposed deviatoric SEF was coupled with the volumetric SEF W_h, defined in Eq. (7), to obtain the complete SEF for inflated membranes. The model parameters have been fitted to the experimental pressure vs. deflection curves, demonstrating the effectiveness of the proposed SEF. In addition, the simulation of the radial stretch was significantly improved compared to the current models. Finally, the results for the transversal stretch further validated the effectiveness of the volumetric SEF W_h in capturing the real volume changes in the materials.

In conclusion, this work brought the following major advancements in the study of inflated membranes:

- Original experimental investigation on inflated circular membranes, providing measurements of the radial stretch and transversal stretch at the pole.
- A novel deviatoric SEF, capable of capturing the mechanics and kinematics of inflated membranes.
- Validation of the volumetric SEF previously developed in Pelliciari et al. (2023) based on simple tension tests. This function captures the real volume changes occurring in elastomers at large deformations.

The proposed SEF can serve as a reference model for characterizing the mechanical response of elastomeric membranes. Although the proposed SEF was specifically calibrated for membrane inflation, where the stress state is typically biaxial, we believe that it possesses all the necessary features for accurate predictions under different stress states. In order to extend the application of the proposed SEF beyond membrane contexts, we recommend validation under compressive and shear stress states, which are not encountered in membrane problems. Additionally, it can be extended to anisotropic materials by including the contribution of anisotropic invariants (Holzapfel and Ogden, 2025), opening up a wide scenario of potential applications such as biological membranes.

CRediT authorship contribution statement

Stefano Sirotti: Writing – review & editing, Writing – original draft, Visualization, Validation, Software, Methodology, Investigation, Formal analysis, Data curation, Conceptualization. **Matteo Pelliciari:** Writing – review & editing, Methodology, Investigation, Data curation, Conceptualization. **Angelo Aloisio:** Investigation, Data curation. **Angelo Marcello Tarantino:** Funding acquisition.

Declaration of competing interest

The authors declare that they have no known competing financial interests or personal relationships that could have appeared to influence the work reported in this paper.

Table A.2
Optimal parameters of the volumetric SEF W_h given by Eq. (7). The parameters were determined in Pelliciari et al. (2023) by fitting the hydrostatic stress given by Eq. (8) to the volumetric curves derived from simple tension tests.

Rubber	κ (MPa)	β_1	β_2	β_3	q
EPDM	490	2.23	9.05	6.88×10^{-4}	0.974
NR	710	7.09	69.25	13.14×10^{-4}	0.723

Table A.3
Optimal parameters obtained by fitting the current deviatoric SEFs to the experimental $\bar{p}$ vs. $\bar{\delta}$ curves. If applicable, the units are in MPa.

Model	EPDM	NR
Yeoh and Fleming (1997)	$A = 0.3$	$A = 0.017$
	$B = 0.004$	$B = 0.10$
	$C_{10} = 0.36$	$C_{10} = 0.33$
	$I_m = 45$	$I_m = 62$
Mooney-Rivlin (Rivlin, 1948)	$C_1 = 0.46$	$C_1 = 0.28$
	$C_2 = 0.074$	$C_2 = 0.017$
Carroll (2011)	$A = 0.3$	$A = 0.21$
	$B = 0.1 \times 10^{-4}$	$B = 0.3 \times 10^{-5}$
	$C = 0.8$	$C = 0.3$
Gent-Gent (Pucci and Saccomandi, 2002)	$C_1 = 0.5$	$C_1 = 0.34$
	$C_2 = 0.45$	$C_2 = -0.09$
	$J_m = 43$	$J_m = 60$
Ogden (1972)	$\mu_1 = 1.3$	$\mu_1 = 0.575$
	$\mu_2 = 4.23 \times 10^{-3}$	$\mu_2 = 5.1 \times 10^{-3}$
	$\alpha_1 = 2.047$	$\alpha_1 = 2.151$
	$\alpha_2 = 6.16$	$\alpha_2 = 5.35$

Table A.4
Optimal parameters of the proposed deviatoric SEF, given by Eq. (9), obtained by fitting the experimental $\bar{p}$ vs. $\bar{\delta}$ curves. If applicable, the units are in MPa.

Model	EPDM	NR
Proposed W_d, Eq. (9)	$A = 0.45$	$A = 0.282$
	$B = 0.0765$	$B = 0.016$
	$I_{2,c} = 93$	$I_{2,c} = 625$
	$(\lambda_c = 3.1)$	$(\lambda_c = 5)$
	$C = 1.376 \times 10^{-5}$	$C = 0.24 \times 10^{-5}$

Acknowledgments

The authors acknowledge the support by the Italian Ministry of University and Research (MUR) through research grants PRIN 2022 PNRR No. P2022AHFCP "New challenges of thin-walled structures at large strains and their promising applications", PRIN 2022 No. P2022ATTAR "Energy harvesting via naturally induced piezoelectric vibration with a view towards application", and FISA-2022 "Earth-Tech" (CUP E93C24000250001). Additional financial support was provided by the University of Modena and Reggio Emilia through the project "FAR Dipartimentale 2024-2025" (CUP E93C24000500005). Support by the National Group of Mathematical Physics (GNFM-INdAM) is also acknowledged. The authors extend their gratitude to Eng. Pasqualino Gualtieri for his valuable assistance in the experiments and to Eng. Giacomo Gramantieri for kindly 3D printing dog-bone-shaped and circular molds.

Appendix A. Fitting parameters

Tables A.2–A.5 list the optimal parameters of the formulations used respectively in Sections 3.1, 4.2, 6 and 6.1.

Appendix B. MATLAB post-processing

This appendix describes the MATLAB post-processing of the videos recorded by the top and lateral cameras during the first test on EPDM and NR membranes. From these elaborations we derived the radial stretch at the pole of the membrane and the deformed shapes, respectively.

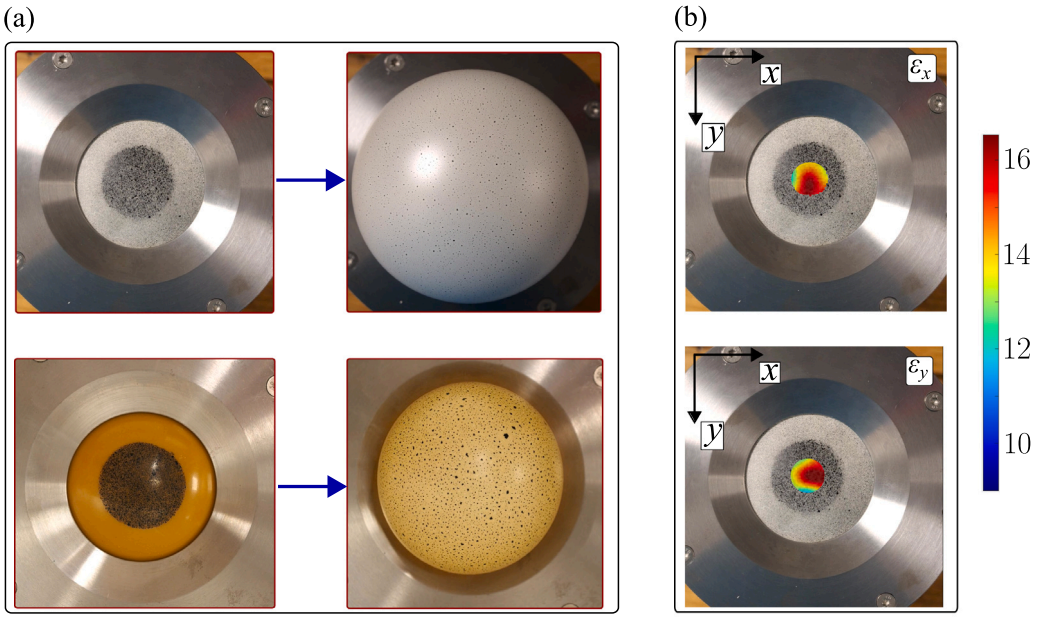

Fig. B.10. DIC analysis using *Ncorr* to determine the radial stretch λ_R at the pole. (a) Two frames extracted from the videos for both EPDM and NR, representing the undeformed configuration and a deformed configuration during the bulge test. (b) Contour plots of Green–Lagrange strains ϵ_x and ϵ_y inside the ROI for EPDM corresponding to the last frame of the test. Due to axial symmetry, these two strain components converge to the same value at the pole.

Table A.5
Optimal parameters of the proposed SEF in case of incompressible materials, Eq. (11). The parameters are obtained by fitting the experimental $\bar{p}$ vs. $\bar{\delta}$ curves. If applicable, the units are in MPa.

Model	EPDM	NR
Incompressible W, Eq. (11)	$A = 0.525$ $B = 0.01575$ $I_{2,c} = 209$ $(\lambda_c = 3.8)$ $C = 0.68 \times 10^{-6}$	$A = 0.287$ $B = 0.01435$ $I_{2,c} = 915$ $(\lambda_c = 5.5)$ $C = 0.95 \times 10^{-6}$

B.1. DIC analysis for the radial stretch at the pole

Before the test, the membrane specimens were prepared with surface patterns to ensure accurate image correlation in the region close to the pole. Specifically, both EPDM an NR membranes were marked with a black pattern. The camera placed above the membrane recorded the first test for both EPDM and NR. We extracted 200 frames from the video and processed them using the *Ncorr* package in MATLAB. Fig. B.10(a) shows two representative frames for both EPDM and NR, illustrating the undeformed configuration and a deformed configuration during inflation.

As shown in Fig. B.10(b), we defined a region of interest (ROI) with a circular shape around the pole. Since the measurements were taken using a single camera, reliable data can only be obtained at the pole, where orthogonality is preserved and the measurements are not affected by the curvature of the deformed membrane. Due to symmetry, at the pole the deformation is equibiaxial, meaning the strains are equal in all directions. A high-strain analysis was performed to compute the Green–Lagrange strain components ϵ_x and ϵ_y during inflation. The resulting contour plot confirms that ϵ_x and ϵ_y attain maximum value at the pole and they are almost identical, as expected. To count for minor discrepancies in the measurements, we considered the average of these values, denoted as ϵ_{max}. The radial stretch at the pole was computed as $\lambda_R = \sqrt{1 + 2\epsilon_{max}}$. Finally, these data were synchronized with the $\bar{p}$ vs. $\bar{\delta}$ curves to obtain the λ_R vs. $\bar{\delta}$ curves displayed in Fig. 3.

B.2. Reconstruction of experimental deformed shapes

The videos recorded by the lateral camera were imported into MATLAB and divided into 50 frames. We developed a MATLAB code capable of identifying the membrane's border by applying a color filter. Fig. B.11(a) shows the deformed profile of the EPDM membrane, as recognized by MATLAB, for two deformed configurations. The distances measured in the frames were converted in real distances by multiplying them by a scaling factor, determined by ensuring that the pole deflection in the last frame matched the final deflection measured by the laser. Fig. B.11(b) shows the reconstructed deformed shapes of EPDM at different values of deflection.

Appendix C. Numerical solution for the inflation of circular membranes

We consider a circular flat membrane with radius L and thickness H. We define a cylindrical coordinate system (R, Θ, Z) with origin in the central point of the membrane. The membrane is inflated under a uniform lateral pressure p and we assume the deformation is axisymmetric. A generic material point $P \equiv (R, \Theta, 0)$ moves to P', with coordinates (r, Θ, z). The principal stretches read

$$\lambda_1 = \lambda_R = \sqrt{r'^2 + z'^2}, \quad \lambda_2 = r/R, \quad \lambda_3 = \lambda_T = h/H, \tag{C.1}$$

where h is the thickness of the membrane in the deformed configuration and the prime denotes differentiation with respect to R.

We consider a hyperelastic material described by a strain energy function $W = W\left(I_1, I_2, I_3\right)$. The principal Cauchy stresses are given by

$$\sigma_i = \frac{1}{\lambda_j \lambda_k} \frac{\partial W}{\partial \lambda_i} = \frac{2\lambda_i}{\lambda_j \lambda_k} \left[w_1 + \left(\lambda_j^2 + \lambda_k^2 \right) w_2 + \lambda_j^2 \lambda_k^2 w_3 \right], \quad i, j, k = 1, 2, 3. \tag{C.2}$$

where $w_i = \partial W / \partial I_i$. In case of a strain energy function written according to the split into the deviatoric and volumetric part, $W = W_d\left(\bar{I}_1, \bar{I}_2\right) + W_h(J)$, the derivatives with respect to the principal invariants are computed with the chain rule. The membrane assumption $\sigma_3 = 0$ determines a relation between the transversal stretch λ_3 and the

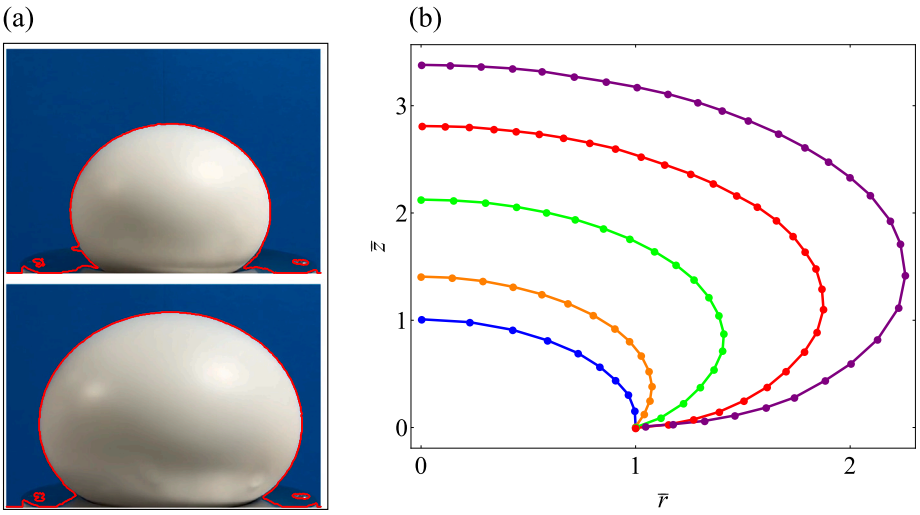

Fig. B.11. MATLAB post-processing of the video recorded by the lateral camera for EPDM. (a) Deformed membranes during the bulge tests. The red curves represent the deformed profiles recognized by MATLAB by differences in color. (b) Reconstructed deformed shapes of EPDM membrane at different values of deflection. The deformed coordinates $\bar{r}$ and $\bar{z}$ are normalized on the radius L. The value $\bar{z}(0)$ corresponds to the normalized deflection $\bar{\delta}$. (For interpretation of the references to color in this figure legend, the reader is referred to the web version of this article.)

principal stretches, λ_1 and λ_2. Except for a few cases of simple energy functions, this relation can be obtained only in implicit form, namely $F(\lambda_1, \lambda_2, \lambda_3) = 0$.

The principal stress resultants per unit length are computed as $T_i = \sigma_i \lambda_3 H$, with $i = 1, 2$. The equilibrium equations in radial and normal directions read

$$\begin{aligned} &\frac{\mathrm{d}T_1}{\mathrm{d}r} + \frac{1}{r}(T_1 - T_2) = 0, \\ &K_1 T_1 + K_2 T_2 = p, \end{aligned} \tag{C.3}$$

where $K_1 = (\lambda_1' \eta - \lambda_1 \eta')/(\lambda_1^2 \sqrt{\lambda_1^2 - \eta^2})$ and $K_2 = (\sqrt{\lambda_1^2 - \eta^2})/(\lambda_1 \lambda_2 R)$ are the principal curvatures, with $\eta = r'$. Substituting the expressions for T_1, T_2, K_1, and K_2 into Eq. (C.3), the following system of differential equations is obtained:

$$\begin{aligned} \lambda_1' &= \frac{\xi_0 + \xi_1 w_1 + \xi_2 w_2 + \xi_3 w_3}{R\lambda_1 \left[w_1 + w_2 \xi_4 + w_3 \xi_5 + \frac{\partial w_1}{\partial \lambda_1} \lambda_1 + \frac{\partial w_2}{\partial \lambda_1} \lambda_1 \left(\lambda_2^2 + \lambda_3^2 \right) + \frac{\partial w_3}{\partial \lambda_1} \lambda_1 \lambda_2^2 \lambda_3^2 \right]}, \\ \lambda_2' &= \frac{\eta - \lambda_2}{R}, \\ \eta' &= \frac{\eta \lambda_1'}{\lambda_1} + \frac{2\zeta_1 \lambda_2 \left(\lambda_1^2 - \eta^2 \right) - \phi \lambda_2 \lambda_1^2 \sqrt{\lambda_1^2 - \eta^2}}{2\zeta_2 \lambda_1^2 R}, \end{aligned} \tag{C.4}$$

where $\phi = pR/H$ and, for the sake of clarity, the following quantities were defined:

$$\begin{aligned} \xi_0 &= \lambda_1^2 \frac{\partial w_1}{\partial \lambda_2} (\lambda_2 - \eta) + \lambda_1^2 \frac{\partial w_2}{\partial \lambda_2} \left(-\eta \lambda_2^2 - \eta \lambda_3^2 + \lambda_2^3 + \lambda_3^2 \lambda_2 \right) \\ &\quad + \lambda_1^2 \lambda_3^2 \lambda_2^2 \frac{\partial w_3}{\partial \lambda_2} (\lambda_2 - \eta), \\ \xi_1 &= \eta \lambda_2 - \lambda_1^2, \\ \xi_2 &= -2 \frac{\partial \lambda_3}{\partial \lambda_2} \eta \lambda_3 \lambda_1^2 + 2 \frac{\partial \lambda_3}{\partial \lambda_2} \lambda_2 \lambda_3 \lambda_1^2 - \eta \lambda_2 \lambda_1^2 + \eta \lambda_2 \lambda_3^2 + \lambda_2^2 \lambda_1^2 - \lambda_3^2 \lambda_1^2, \\ \xi_3 &= -2 \frac{\partial \lambda_3}{\partial \lambda_2} \eta \lambda_1^2 \lambda_3 \lambda_2^2 + 2 \frac{\partial \lambda_3}{\partial \lambda_2} \lambda_1^2 \lambda_3 \lambda_2^3 - \eta \lambda_1^2 \lambda_3^2 \lambda_2 + \lambda_1^2 \lambda_3^2 \lambda_2^2, \\ \xi_4 &= 2 \frac{\partial \lambda_3}{\partial \lambda_1} \lambda_1 \lambda_3 + \lambda_2^2 + \lambda_3^2, \\ \xi_5 &= 2 \frac{\partial \lambda_3}{\partial \lambda_1} \lambda_1 \lambda_3 \lambda_2^2 + \lambda_3^2 \lambda_2^2, \\ \zeta_1 &= w_1 + \lambda_1^2 w_2 + \lambda_3^2 \left(\lambda_1^2 w_3 + w_2 \right), \\ \zeta_2 &= w_1 + \lambda_2^2 w_2 + \lambda_3^2 \left(\lambda_2^2 w_3 + w_2 \right). \end{aligned} \tag{C.5}$$

The derivatives of λ_3 with respect to λ_1 and λ_2 must be computed numerically by means of the implicit function theorem, namely

$$\frac{\partial \lambda_3}{\partial \lambda_1} = -\frac{\partial F/\partial \lambda_1}{\partial F/\partial \lambda_3}, \quad \frac{\partial \lambda_3}{\partial \lambda_2} = -\frac{\partial F/\partial \lambda_2}{\partial F/\partial \lambda_3}. \tag{C.6}$$

System (C.4) must be integrated from the pole to the outer boundary, satifying initial conditions for $\lambda_1, \lambda_2, \eta$ at the pole and the supplementary condition $\lambda_2(L) = 1$ at the outer boundary. The numerical integration was performed by function *ode45* on MATLAB by following these steps: (i) set an initial condition λ_0 for $\lambda_1, \lambda_2, \eta$ at the pole and a guess value p_0 for the pressure; (ii) the initial value for λ_3 is computed solving numerically the membrane assumption $\sigma_3 = 0$ at the pole; (iii) compute consequently $\partial\lambda_3/\partial\lambda_1$, $\partial\lambda_3/\partial\lambda_2$, $\partial w_1/\partial\lambda_1$, $\partial w_1/\partial\lambda_2$, $\partial w_2/\partial\lambda_1$, $\partial w_2/\partial\lambda_2$, $\partial w_3/\partial\lambda_1$ and $\partial w_3/\partial\lambda_2$; (iv) the values of λ_1, λ_2 and η at the next point of the domain are computed from system (C.4); (v) steps (ii), (iii) and (iv) are repeated for each point along the domain until $\lambda_2 = 1$. The value of R at which $\lambda_2 = 1$ is denoted by R^*; (vi) in general, R^* will not coincide with L since the initial guess value p_0 is not the correct pressure. However, system (C.4) is invariant when a scaling factor is multiplied to R (Yang and Feng, 1970). Hence, choosing $\gamma = L/R^*$ as scaling factor it is possible to compute the correct value of pressure as $p = p_0/\gamma = p_0 R^*/L$; (vii) perform again the numerical integration with the correct value p, obtain the correct stretches profiles λ_1 and λ_2. The deformed coordinates r and z are computed by Eq. (C.1). In particular, the value of z at $R = 0$ corresponds to the deflection of the pole δ; (viii) repeat this procedure for different initial conditions λ_0 to derive the entire pressure curve.

The optimization of model parameters was carried out on MATLAB as well. The experimental $\bar{p}$ vs. $\bar{\delta}$ curves were imported as discretized pairs $\bar{p}_i$, $\bar{\delta}_i$. The constitutive parameters of the proposed deviatoric SEF were gathered in the parameter vector $\boldsymbol{\theta} = [A, B, I_{2,c}, C]$. The initial guess for the parameters was determined manually as described in Section 5. The objective function was defined as the squared root of the sum of squared relative residuals between the experimental and simulated pressure:

$$\mathrm{obj}(\boldsymbol{\theta}) = \sqrt{\sum_i^n \left(\frac{\bar{p}(\bar{\delta}_i, \boldsymbol{\theta}) - \bar{p}_i}{\bar{p}_i} \right)^2}, \tag{C.7}$$

where n is the number of points considered in the fitting. To perform the minimization of Eq. (C.7) we adopted the function *patternsearch*.

$$
\begin{aligned}
\lambda_1' &= \frac{w_1\psi_1 + w_2\psi_2 + \frac{\partial w_1}{\partial \lambda_2}\psi_3 + \frac{\partial w_2}{\partial \lambda_2}\psi_4}{R\lambda_2\left[3w_1 - \frac{\partial w_1}{\partial \lambda_1}\lambda_1 + \left(3w_2 - \frac{\partial w_2}{\partial \lambda_1}\lambda_1 + w_1\lambda_1^4 + \frac{\partial w_1}{\partial \lambda_1}\lambda_1^5\right)\lambda_2^2 + \lambda_1^4\left(w_2 + \frac{\partial w_2}{\partial \lambda_1}\lambda_1\right)\lambda_2^4\right]},\\
\lambda_2' &= \frac{\eta - \lambda_2}{R},\\
\eta' &= \frac{\eta\lambda_1'}{\lambda_1} - \frac{\phi\lambda_1^5\lambda_2^4\sqrt{-\eta^2+\lambda_1^2} + 2\lambda_1\left(\eta^2 - \lambda_1^2\right)\left(w_1 + w_2\lambda_1^2\right)\left(\lambda_1^2\lambda_2^4 - 1\right)}{2R\lambda_1\lambda_2\left(w_1 + w_2\lambda_2^2\right)\left(\lambda_1^4\lambda_2^2 - 1\right)},
\end{aligned}
\tag{C.9}
$$

Box I.

Contrary to traditional algorithms such as *fmincon*, *patternsearch* does not require gradient information. This makes it particularly suitable for optimizing objective functions defined through numerically solved ODEs, where analytical gradients are not readily available. On the other hand, *patternsearch* was preferred over genetic algorithms due to the small dimension of the parameter vector.

C.1. Solution for incompressible materials

In case of incompressible materials, the deformation is isochoric, $I_3 = 1$, and the SEF depends only on the first and second invariants of strain, $W = W(I_1, I_2)$. The principal stretches λ_1 and λ_2 are given in Eq. (C.1), whereas the transversal stretch is computed by the incompressibility constraint, namely $\lambda_3 = 1/(\lambda_1\lambda_2)$. The principal Cauchy stresses read

$$
\sigma_i = 2\left(w_1 + \lambda_j^2 w_2\right)\left(\lambda_i^2 - \frac{1}{\lambda_i^2\lambda_j^2}\right), \quad i,j = 1,2, \tag{C.8}
$$

and the principal stress resultants are computed as $T_i = \sigma_i H/(\lambda_i\lambda_j)$ for $i,j = 1,2$. Using the equilibrium Eqs. (C.3), the following system of differential equations is obtained (Sirotti et al., 2024) (see Eq. (C.9) which is given in Box I), where $\phi = pR/H$ and, for the sake of clarity, the following quantities were defined:

$$
\begin{aligned}
\psi_1 &= \eta\lambda_2^4\lambda_1^3 - 3\eta\lambda_1 - \lambda_2^3\lambda_1^5 + 3\lambda_2\lambda_1,\\
\psi_2 &= -\eta\lambda_2^4\lambda_1^5 - \eta\lambda_1^3 + \lambda_2^5\lambda_1^5 + \lambda_2^3\lambda_1,\\
\psi_3 &= -\eta\lambda_2^3\lambda_1^5 + \eta\lambda_2\lambda_1 + \lambda_2^4\lambda_1^5 - \lambda_2^2\lambda_1,\\
\psi_4 &= -\eta\lambda_1^5\lambda_2^5 + \eta\lambda_1\lambda_2^3 + \lambda_1^5\lambda_2^6 - \lambda_1\lambda_2^4.
\end{aligned}
\tag{C.10}
$$

Data availability

Data will be made available on request.

References

Adkins, J.E., Rivlin, R.S., 1952. Large elastic deformations of isotropic materials IX. The deformation of thin shells. Philos. Trans. R. Soc. Lond. Ser. A Math. Phys. Sci. 244 (888), 505–531.

Anssari-Benam, A., 2021. On a new class of non-Gaussian molecular-based constitutive models with limiting chain extensibility for incompressible rubber-like materials. Math. Mech. Solids 26 (11), 1660–1674.

Anssari-Benam, A., 2023. Continuous softening up to the onset of failure: A hyperelastic modelling approach with intrinsic softening for isotropic incompressible soft solids. Mech. Res. Commun. 132, 104183.

Anssari-Benam, A., Bucchi, A., Saccomandi, G., 2021. On the central role of the invariant I_2 in nonlinear elasticity. Internat. J. Engrg. Sci. 163, 103486.

Anssari-Benam, A., Saccomandi, G., 2024. Continuous softening as a state of hyperelasticity: Examples of application to the softening behavior of the brain tissue. J. Biomech. Eng. 146 (9).

Arruda, E.M., Boyce, M.C., 1993. A three-dimensional constitutive model for the large stretch behavior of rubber elastic materials. J. Mech. Phys. Solids 41 (2), 389–412.

Blatz, P.J., Ko, W.L., 1962. Application of finite elastic theory to the deformation of rubbery materials. Trans. Soc. Rheol. 6 (1), 223–252.

Borjalilou, V., Asghari, M., 2022. Mathematical modeling of anisotropic hyperelastic cylindrical thick shells by incorporating thickness deformation and compressibility with application to arterial walls. Int. J. Struct. Stab. Dyn. 22 (13), 2250141.

Boyce, M.C., Arruda, E.M., 2000. Constitutive models of rubber elasticity: a review. Rubber Chem. Technol. 73 (3), 504–523.

Carroll, M.M., 2011. A strain energy function for vulcanized rubbers. J. Elasticity 103, 173–187.

Chaudhuri, A., DasGupta, A., 2014. On the static and dynamic analysis of inflated hyperelastic circular membranes. J. Mech. Phys. Solids 64, 302–315.

Chen, L., Chen, W., Xue, Y., Zhang, M., Chen, X., Cao, X., Zhang, Z., Li, G., Li, T., 2019. Investigation of the state transition and moving boundary in a pneumatic–hydraulic coupled dielectric elastomer actuator. J. Appl. Mech. 86 (3), 031004.

Destrade, M., Saccomandi, G., Sgura, I., 2017. Methodical fitting for mathematical models of rubber-like materials. Proc. R. Soc. A: Math. Phys. Eng. Sci. 473 (2198), 20160811.

Doutres, O., Atalla, N., Dong, K., 2011. Effect of the microstructure closed pore content on the acoustic behavior of polyurethane foams. J. Appl. Phys. 110 (6).

Falope, F.O., Lanzoni, L., Tarantino, A.M., 2024. Energetic exhaustiveness for the direct characterization of energy forms of hyperelastic isotropic materials. J. Mech. Phys. Solids 193, 105885.

Fichter, W.B., 1997. Some Solutions for the Large Deflections of Uniformly Loaded Circular Membranes. Vol. 3658, National Aeronautics and Space Administration, Langley Research Center.

Gent, A., 2005. Extensibility of rubber under different types of deformation. J. Rheol. 49 (1), 271–275.

Gorissen, B., Milana, E., Baeyens, A., Broeders, E., Christiaens, J., Collin, K., Reynaerts, D., De Volder, M., 2019. Hardware sequencing of inflatable nonlinear actuators for autonomous soft robots. Adv. Mater. 31 (3), 1804598.

Hailan, S.M., Ponnamma, D., Krupa, I., 2021. The separation of oil/water mixtures by modified melamine and polyurethane foams: A review. Polymers 13 (23), 4142.

Holzapfel, G.A., Ogden, R.W., 2025. Modeling the biomechanical properties of soft biological tissues: Constitutive theories. Eur. J. Mech. A Solids 112, 105634.

Horgan, C.O., Saccomandi, G., 2002. A molecular-statistical basis for the gent constitutive model of rubber elasticity. J. Elasticity 68, 167–176.

Horgan, C.O., Smayda, M.G., 2012. The importance of the second strain invariant in the constitutive modeling of elastomers and soft biomaterials. Mech. Mater. 51, 43–52.

Huntington, C.G., 2013. Tensile Fabric Structures: Design, Analysis, and Construction. American Society of Civil Engineers.

Jenkins, C.H.M., 2001. Gossamer Spacecraft: Membrane and Inflatable Structures Technology for Space Applications. American Institute of Aeronautics and Astronautics.

Jones, W.V., 2014. Evolution of scientific ballooning and its impact on astrophysics research. Adv. Space Res. 53 (10), 1405–1414.

Kawabata, S., Kawai, H., 2005. Strain energy density functions of rubber vulcanizates from biaxial extension. In: Molecular Properties. Springer, pp. 89–124.

Khiêm, V.N., Itskov, M., 2016. Analytical network-averaging of the tube model:: Rubber elasticity. J. Mech. Phys. Solids 95, 254–269.

Koh, S.J.A., Keplinger, C., Li, T., Bauer, S., Suo, Z., 2010. Dielectric elastomer generators: How much energy can be converted? IEEE/ASME Trans. Mechatronics 16 (1), 33–41.

Kugler, H.P., Stacer, R.G., Steimle, C., 1990. Direct measurement of Poisson's ratio in elastomers. Rubber Chem. Technol. 63 (4), 473–487.

Kuznetsov, S.V., 2024. Torsional waves in hyperelastic shells: Appearing shock waves and energy dissipation. Mech. Mater. 189, 104905.

Li, T., Keplinger, C., Baumgartner, R., Bauer, S., Yang, W., Suo, Z., 2013. Giant voltage-induced deformation in dielectric elastomers near the verge of snap-through instability. J. Mech. Phys. Solids 61 (2), 611–628.

Li, Y., Nemes, J.A., Derdouri, A.A., 2001. Membrane inflation of polymeric materials: Experiments and finite element simulations. Polym. Eng. Sci. 41 (8), 1399–1412.

Liu, Z., McBride, A., Sharma, B.L., Steinmann, P., Saxena, P., 2021. Coupled electro-elastic deformation and instabilities of a toroidal membrane. J. Mech. Phys. Solids 151, 104221.

Liu, M.X., Wang, C.G., Li, X.D., 2018. Rigid-flexible contact analysis of an inflated membrane balloon with various contact conditions. Int. J. Solids Struct. 144, 218–229.
Ma, C., Gao, J., Wang, D., Yuan, Y., Wen, J., Yan, B., Zhao, S., Zhao, X., Sun, Y., Wang, X., et al., 2019. Sunlight polymerization of poly (amidoxime) hydrogel membrane for enhanced uranium extraction from seawater. Adv. Sci. 6 (13), 1900085.
Ma, R.Q., Wei, J.Z., Tan, H.F., Yang, Z.H., 2018. Modal analysis of inflated membrane cone considering pressure follower force effect. Thin-Walled Struct. 132, 596–603.
Machado, G., Favier, D., Chagnon, G., 2012. Membrane curvatures and stress-strain full fields of axisymmetric bulge tests from 3D-DIC measurements. Theory and validation on virtual and experimental results. Exp. Mech. 52, 865–880.
McKenna, G.B., 2018. Soft matter: rubber and networks. Rep. Progr. Phys. 81 (6), 066602.
Miehe, C., Göktepe, S., Lulei, F., 2004. A micro-macro approach to rubber-like materials - part I: the non-affine micro-sphere model of rubber elasticity. J. Mech. Phys. Solids 52 (11), 2617–2660.
Moerman, K.M., Fereidoonnezhad, B., McGarry, J.P., 2020. Novel hyperelastic models for large volumetric deformations. Int. J. Solids Struct. 193, 474–491.
Murphy, J., Rajagopal, K., 2021. Inflation of residually stressed fung-type membrane models of arteries. J. Mech. Behav. Biomed. Mater. 122, 104699.
Ogden, R.W., 1972. Large deformation isotropic elasticity–on the correlation of theory and experiment for incompressible rubberlike solids. Proc. R. Soc. A 326 (1567), 565–584.
Ogden, R.W., 1997. Non-Linear Elastic Deformations. Courier Corporation.
Ogden, R.W., Saccomandi, G., Sgura, I., 2004. Fitting hyperelastic models to experimental data. Comput. Mech. 34, 484–502.
Pamplona, D., Mota, D., 2012. Numerical and experimental analysis of inflating a circular hyperelastic membrane over a rigid and elastic foundation. Int. J. Mech. Sci. 65 (1), 18–23.
Patil, A., DasGupta, A., 2013. Finite inflation of an initially stretched hyperelastic circular membrane. Eur. J. Mech. A Solids 41, 28–36.
Patil, A., DasGupta, A., Eriksson, A., 2015. Contact mechanics of a circular membrane inflated against a deformable substrate. Int. J. Solids Struct. 67, 250–262.
Pelliciari, M., Sirotti, S., Aloisio, A., Tarantino, A.M., 2022. Analytical, numerical and experimental study of the finite inflation of circular membranes. Int. J. Mech. Sci. 226, 107383.
Pelliciari, M., Sirotti, S., Aloisio, A., Tarantino, A.M., 2025. Hyperelastic model for nonlinear elastic deformations of graphene-based polymer nanocomposites. Int. J. Solids Struct. 308, 113144.
Pelliciari, M., Sirotti, S., Tarantino, A.M., 2023. A strain energy function for large deformations of compressible elastomers. J. Mech. Phys. Solids 176, 105308.
Pucci, E., Saccomandi, G., 2002. A note on the gent model for rubber-like materials. Rubber Chem. Technol. 75 (5), 839–852.
Reddy, N.H., Saxena, P., 2017. Limit points in the free inflation of a magnetoelastic toroidal membrane. Int. J. Non-Linear Mech. 95, 248–263.
Rivlin, R.S., 1948. Large elastic deformations of isotropic materials IV. Further developments of the general theory. Philos. Trans. R. Soc. Lond. Ser. A Math. Phys. Sci. 241 (835), 379–397.
Rivlin, R.S., Saunders, D., 1951. Large elastic deformations of isotropic materials VII. Experiments on the deformation of rubber. Philos. Trans. R. Soc. Lond. Ser. A Math. Phys. Sci. 243 (865), 251–288.
Sansour, C., 2008. On the physical assumptions underlying the volumetric-isochoric split and the case of anisotropy. Eur. J. Mech. A Solids 27 (1), 28–39.
Sedighi, F., Darijani, H., Darijani, F., 2021. A novel phenomenological viewpoint for transversely isotropic hyperelastic materials; a new strain energy density function. Int. J. Solids Struct. 225, 111064.
Serina, E.R., Mockensturm, E., Mote, Jr., C.D., Rempel, D., 1998. A structural model of the forced compression of the fingertip pulp. J. Biomech. 31 (7), 639–646.
Sheng, J.Y., Zhang, L.Y., Li, B., Wang, G.F., Feng, X.Q., 2017. Bulge test method for measuring the hyperelastic parameters of soft membranes. Acta Mech. 228, 4187–4197.
Sirotti, S., Pelliciari, M., Aloisio, A., Tarantino, A.M., 2023. Analytical pressure–deflection curves for the inflation of pre-stretched circular membranes. Eur. J. Mech. A Solids 97, 104831.
Sirotti, S., Pelliciari, M., Tarantino, A.M., 2024. Effect of compressibility on the mechanics of hyperelastic membranes. Int. J. Mech. Sci. 109441.
Starkova, O., Aniskevich, A., 2010. Poisson's ratio and the incompressibility relation for various strain measures with the example of a silica-filled SBR rubber in uniaxial tension tests. Polym. Test. 29 (3), 310–318.
Stewart, B.G., Sitaraman, S.K., 2021. Biaxial inflation stretch test for flexible electronics. Adv. Eng. Mater. 2001503.
Takashima, K., Kitou, T., Mori, K., Ikeuchi, K., 2007. Simulation and experimental observation of contact conditions between stents and artery models. Med. Eng. Phys. 29 (3), 326–335.
Tamadapu, G., DasGupta, A., 2014. Effect of curvature and anisotropy on the finite inflation of a hyperelastic toroidal membrane. Eur. J. Mech. A Solids 46, 106–114.
Tamura, H., Furuike, T., Nair, S., Jayakumar, R., 2011. Biomedical applications of chitin hydrogel membranes and scaffolds. Carbohydr. Polymers 84 (2), 820–824.
Upadhyay, K., Subhash, G., Spearot, D., 2019. Thermodynamics-based stability criteria for constitutive equations of isotropic hyperelastic solids. J. Mech. Phys. Solids 124, 115–142.
Vandeparre, H., Watson, D., Lacour, S., 2013. Extremely robust and conformable capacitive pressure sensors based on flexible polyurethane foams and stretchable metallization. Appl. Phys. Lett. 103 (20).
Volokh, K.Y., 2004. Nonlinear elasticity for modeling fracture of isotropic brittle solids. J. Appl. Mech. 71 (1), 141–143.
Volokh, K.Y., 2007. Hyperelasticity with softening for modeling materials failure. J. Mech. Phys. Solids 55 (10), 2237–2264.
Volokh, K.Y., 2010. On modeling failure of rubber-like materials. Mech. Res. Commun. 37 (8), 684–689.
Wagner, M., 1994. The origin of the C_2 term in rubber elasticity[a]. J. Rheol. 38 (3), 655–679.
Walker, J., Zidek, T., Harbel, C., Yoon, S., Strickland, F.S., Kumar, S., Shin, M., 2020. Soft robotics: a review of recent developments of pneumatic soft actuators. In: Actuators. Vol. 9, Multidisciplinary Digital Publishing Institute, p. 3.
Wang, H.Y., Zhang, Y.Q., 2014. Processing and characterisation of a novel electropolymerized silk fibroin hydrogel membrane. Sci. Rep. 4 (1), 6182.
Wineman, A., 2005. Some results for generalized neo-Hookean elastic materials. Int. J. Non-Linear Mech. 40 (2–3), 271–279.
Yang, W.H., Feng, W.W., 1970. On axisymmetrical deformations of nonlinear membranes. J. Appl. Mech. 37 (4), 1002–1011.
Yang, X., Yu, L., Long, R., 2021. Contact mechanics of inflated circular membrane under large deformation: Analytical solutions. Int. J. Solids Struct. 233, 111222.
Yazdi, M.K., Vatanpour, V., Taghizadeh, A., Taghizadeh, M., Ganjali, M.R., Munir, M.T., Habibzadeh, S., Saeb, M.R., Ghaedi, M., 2020. Hydrogel membranes: A review. Mater. Sci. Eng.: C 114, 111023.
Yeoh, O.H., Fleming, P.D., 1997. A new attempt to reconcile the statistical and phenomenological theories of rubber elasticity. J. Polym. Sci. Part B: Polym. Phys. 35 (12), 1919–1931.
Yohsuke, B., Urayama, K., Takigawa, T., Ito, K., 2011. Biaxial strain testing of extremely soft polymer gels. Soft Matter 7 (6), 2632–2638.
Yuan, J., Liu, X., Xia, H., Huang, Y., 2021. Analytical solutions for inflation of pre-stretched elastomeric circular membranes under uniform pressure. Theor. Appl. Mech. Lett. 100243.